ADVANCED FUNCTIONAL MATERIALS
www.afm-journal.de

Pressure-Induced Capacity Recovery and Performance Enhancements in LTO/NMC-LCO Batteries

Ahmed Chahbaz, Yucheng Luo, Gereon Stahl, Heinrich Ditler, Tony Jaumann, Martin Glinka, Christian Lingen, Dirk Uwe Sauer, and Weihan Li*

Lithium titanate oxide (LTO) batteries are a promising technology, particularly suitable for high-power applications, owing to their inherent cyclic stability, fast charging capability, and superior safety. However, substantial gas generation and accelerated aging driven by the cathode remain substantial challenges. This study explores the mitigation of these aging mechanisms through the application of external mechanical compression. Continuous pressure of 0.3 MPa applied to pristine cells during cycling reduces capacity loss by 42% compared to unpressurized cells cycled under identical operating conditions. Applying short-term pressure to aged cells leads to immediate capacity recovery, reclaiming up to 57% of the lost capacity. Subsequent cycling of these aged cells under continuous pressure demonstrates improved capacity retention. In contrast, intermittently applied transient pressure causes notable capacity fluctuations. This study reveals insights into aging and healing mechanisms influenced by external pressure, benefiting both first- and second-life battery applications. Understanding these mechanisms is vital for enhancing performance and lifetime in battery packs, while the findings also highlight promising opportunities for capacity recovery in reused batteries.

1. Introduction

The excessive use of fossil fuels and subsequent greenhouse gas emissions have led to an abnormal increase in carbon dioxide (CO_2) concentration in the atmosphere since 1950.[1] Hence, CO_2 emission-reducing innovations, especially in the field of battery-powered mobility, have been subject to many applications and studies in recent years.[2,3] The high energy and power density, the high coulombic efficiency, as well as the low self-discharge rate and low maintenance costs, have made lithium-ion batteries (LIB) predominant in the field of large-scale applications such as electric vehicles and energy storage systems.[4]

Since the emergence of LIBs, a lot of effort has been put into studying potential performance-improving factors with regard to energy and power capability.[5,6] Different approaches at diverse levels of abstraction in various calendar and cyclic aging studies focus on parameters such as the influence of temperature, depth of discharge (DOD), state of charge (SOC), C-rate and their interplay on cell aging.[7–12] However, in the context of battery pack design for traction applications, the parameter of pressure, although often neglected in cycle and calendar lifetime studies, is of great importance with regards to inhomogeneous aging at the cell level as well as mechanical pack stability and safety.[13,14]

Previous studies on pouch cells revealed that a small amount of external mechanical compression can enhance initial capacity extraction and long-term performance of LIBs. Cannarella et al., investigated the influence of pressure on capacity loss by initially applying varying degrees of external compression on constrained cells.[15] A small amount of mechanical compression was found to benefit long-term performance by preventing electrode detachment and thus decreasing contact loss. However, excessive pressure led to an accelerated capacity fade attributed to loss of lithium inventory (*LLI*), as confirmed by post-mortem analysis. This aligns with the findings of Mussa et al., who additionally suggest the existence of an optimum pressure that extends cycle life by reducing *LLI*.[16] Müller et al., demonstrated that the absence of uniform pressure distribution during cycling results in pronounced lithium deposition and inhomogeneous aging behavior.[17] Berckmans et al., found that the application of external pressure led to a significant increase in extracted capacity and a decrease in ohmic resistance compared to unpressurized

A. Chahbaz, Y. Luo, G. Stahl, H. Ditler, D. U. Sauer, W. Li
Chair for Electrochemical Energy Conversion and Storage Systems (ESS)
Institute for Power Electronics and Electrical Drives (ISEA), RWTH Aachen University
Campus-Boulevard 89, 52074 Aachen, Germany
E-mail: ahmed.chahbaz@isea.rwth-aachen.de

A. Chahbaz, Y. Luo, G. Stahl, H. Ditler, D. U. Sauer, W. Li
Center for Aging
Reliability and Lifetime Prediction of Electrochemical and Power Electronic Systems (CARL)
Campus-Boulevard 89, 52074 Aachen, Germany

A. Chahbaz, Y. Luo, G. Stahl, H. Ditler, D. U. Sauer, W. Li
Jülich Aachen Research Alliance, JARA-Energy
Templergraben 55, 52056 Aachen, Germany

T. Jaumann, M. Glinka, C. Lingen
Siemens Mobility GmbH
Siemenspromenade 4, 91058 Erlangen, Germany

D. U. Sauer
Helmholtz Institute Münster (HI MS)
IEK-12, Forschungszentrum Jülich, 52425 Jülich, Germany

The ORCID identification number(s) for the author(s) of this article can be found under https://doi.org/10.1002/adfm.202419229

DOI: 10.1002/adfm.202419229

cells.[18] Besides pouch cells, prismatic cells are commonly used in electric vehicles, providing various advantages in terms of mechanical stiffness and efficient packaging.[19] However, currently, there are only a few studies that focus on the effects of applied external pressure on prismatic cells. Daubinger et al. investigated the positive impact of external mechanical compression on large-format prismatic cells.[20] Applying pressure to the cells significantly extended their lifespan in comparison to cells that were not pressurized. Furthermore, although the overall performance of the cell improved due to reduced lithium plating caused by the anode, the cathode experienced more significant structural damage due to pressurization.

The potentially significant influence of externally applied pressure on prismatic cells underlines the necessity for further studies. Notably, existing research concerning the effects of external pressure on LIBs has primarily focused on graphite or silicon-based cells. There, external pressure is applied in order to counteract the volume expansion of these materials during lithiation/delithiation.[21,22] Hence, to the best of our knowledge, this study represents the first investigation into the effects of externally applied pressure on prismatic cells with lithium titanate oxide (LTO) as anode material. The unique zero-strain characteristic of LTO and the higher anode potential of 1.55 V versus Li/Li^+ makes it less susceptible to the formation of a solid electrolyte interface (SEI) and lithium plating compared to graphite anodes.[23,24] However, severe gassing, poor electronic conductivity in the spinel $Li_4Ti_5O_{12}$ phase, and sluggish lithium diffusion properties present major drawbacks for the technology at hand.[25–27] Devie et al. investigated an overcharged LTO/NMC cell, observing increased capacity degradation coupled with pronounced gas generation following the overcharge event.[28] They attributed the degradation to localized gas pockets, which resulted in the displacement of liquid electrolyte and mechanical separation of opposite electrode regions. Similarly to applying external pressure, they massaged the cell and restored nearly 60% of the lost capacity back by laterally displacing the accumulated gas and reconnecting the separated active material, showcasing the potential of external pressure to recover a significant portion of lost capacity within LTO batteries.[29] Mao et al. reported similar findings in their work.[30] Applying pressure to aged graphite/NMC-LMO cells resulted in substantial capacity recovery. Their analysis indicated that previously generated gaseous substances caused local dry-out of active material on both electrodes by blocking ionic pathways. Both studies indicate a reversible capacity loss that can be recovered by applying external pressure to the cell. Matadi et al. observed round-shaped spots on both the electrodes and the separator, inferring that these spots indicated separated electrode regions due to gas generation.[31] Bank et al. identified similar dark spots on a LTO/NMC battery during optical examination of the extracted anode and cathode material.[32] In particular, these spots were localized in areas where gas bubbles had been observed earlier. These collective findings emphasize the critical importance of evaluating the effects of external pressurization and its correlation with gassing behavior in LTO batteries.

In this work, we investigate the impact of various externally applied pressurization methods on pristine and aged prismatic LTO batteries by analyzing occurring degradation modes and deriving physical explanations based on electrochemical impedance spectroscopy (EIS) and post-mortem analysis. The aforementioned zero-strain LTO characteristic implies that external pressure may have a limited effect, since it does not mitigate any inherent volume changes. However, as demonstrated in our study, external pressure provides substantial benefits for LTO-based batteries, and this paper is the first to present empirical evidence to support these findings. Initially, we demonstrate the beneficial impact of a continuously applied pressure of 0.3 MPa during cycling on pristine cells and compare it to the aging behavior of similarly operated cells without external pressurization. We find that the application of long-term continuous external pressure reduces capacity loss by 42% compared to unpressurized cycling. Subsequently, transient pressure is temporarily applied to 36 previously unpressurized aged cells to analyze potential capacity recovery effects. We report that applying short-term transient external pressure to aged cells results in an immediate capacity recovery of up to 57% of the prior lost capacity. The six most affected cells by transient pressure, in terms of capacity recovery, are then further cycled under continuous pressure to assess the long-term sustainability of the observed capacity recovery. Furthermore, intermittently applied transient pressure on these cells is investigated. Our results show that further cycling under continuous pressure for these aged cells shows improved capacity retention by reducing cathode degradation, while intermittently applied transient pressure results in significant capacity fluctuations.

2. Results and Discussion

2.1. Continuous External Pressure on Pristine Cells

In **Figure 1a** the cyclic aging results for continuously pressurized and unpressurized cells are depicted. It becomes visible that the pressurized cells exhibit a less pronounced capacity fade compared to the unpressurized cells. After 8000 equivalent full cycles (EFC) the pressurized cells showed a state of health (SOH) of 90.8% (specimen 1), respectively 90.4% (specimen 2), whereas the extracted capacity of the unpressurized cells had already decreased to 84.1% (specimen 1), respectively 83.3% (specimen 2). All SOH values are related to the initial capacity as per Equation (4). Furthermore, considering the internal resistance in Figure 1b, the positive influence of pressurization becomes even more evident. For the unpressurized cells, the internal resistance showed a relative increase of 59.7% (specimen 1), respectively 85.4% (specimen 2) after 8000 EFC, while only a minor increase in internal resistance below 3% became visible for both pressurized specimens. The stronger positive influence of pressurization on resistance characteristics is in agreement with the results for graphite-based batteries of Berckmans et al.[18]

In order to examine the distinct influence of each electrode component on aging, first the cathode blend characteristic is simulated.[33,34] Therefore, coin-cell measurements in half-cell configuration are conducted on the individual cathode materials of the investigated blend, i.e., LCO versus Li/Li^+ and NMC versus Li/Li^+. The results are then used to mimic the real behavior of the given NMC-LCO cathode blend on the basis of harvested pristine cathode material extracted upon cell opening. For additional information on the coin cell preparation, the reader is referred to the experimental Section 4. As the incremental capacity

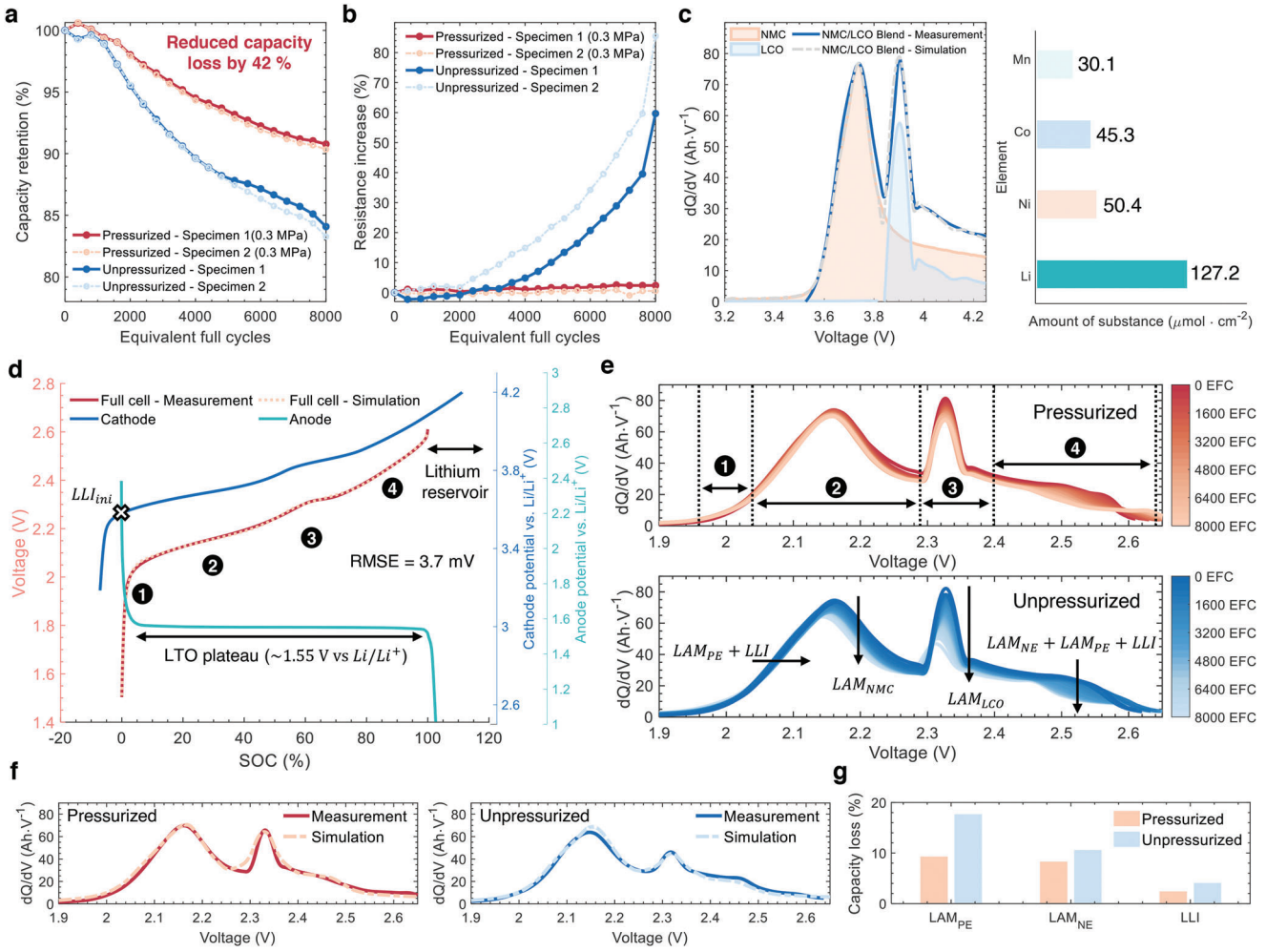

Figure 1. a) Capacity and b) Resistance development for cells cycled in pressurized (red) and unpressurized (blue) condition with DOD= 80% at 3C and 45°C. c) IC curves of the pristine measured and simulated cathode blend using individual LCO and NMC half-cell measurements and results of the ICP-OES measurement. d) Full-cell voltage reconstruction by means of electrode balancing for a pristine cell. e) IC curve progression over aging for specimen 1 in pressurized (red), and unpressurized (blue) condition. f) Measured and simulated IC curve after 8000 EFC for specimen 1 in pressurized (red) and unpressurized (blue) condition. g) Results of the degradation mode analysis for LAM_{PE}, LAM_{NE} and LLI.

(IC) curve is additive for each component, the blend characteristic can be calculated as following:

$$\frac{dQ}{dV}|_{Blend} = \alpha \cdot \frac{dQ}{dV}|_{NMC} + \beta \cdot \frac{dQ}{dV}|_{LCO} \quad (1)$$

α and β define the fraction of the respective blend component capacity on the overall blend cathode capacity. They are obtained by minimizing the RMSE between the measured IC curve of the NMC-LCO blend cathode from the harvested pristine cathode material and the simulated IC curve based on Equation (1) for the individual blend components. The IC curves obtained from the pristine cathode blend and the simulated blend are presented in Figure 1c. It becomes visible that the simulated and measured cathode blend are in good agreement by comparing the peak position and intensity of the respective IC curves. The occurring distinct features in the IC curves are assigned to the specific cathode material component under consideration of their electrochemical properties. It becomes evident that the visible peak at 3.7 V versus Li/Li^+ (~2.15 V versus LTO) is attributed to the NMC portion of the cathode blend. Similarly, the IC peak at 3.9 V versus Li/Li^+ (~2.35 V versus LTO) is associated with the LCO component of the cathode blend. Furthermore, a superposed effect of the NMC capacity within the LCO voltage region exists, affecting the peak height to a certain extent. The voltage region between 4 and 4.25 V versus Li/Li^+ is influenced by both the LCO and NMC capacity, whereas the NMC capacity accounts for a larger share. Based on the initial fit, a blend ratio of 75% NMC and 25% LCO is determined, which is a reasonable ratio, considering the results from ICP-OES measurements as provided in Figure 1c. These results are further supported by SEM-EDX measurements, which will be presented in Section 2.3.

Subsequently, the pristine full-cell voltage is reconstructed by means of electrode balancing, as illustrated in Figure 1d. This is achieved by matching the potential difference between the cathode and anode half-cell curves with the pristine full-cell voltage

Table 1. Overview of the shifts in IC characteristics (1)–(4) for different separately simulated degradation modes, based on the results from Figure S1 (Supporting Information).

Degradation Modes	Region (1)	Region (2)	Region (3)	Region (4)
LLI	⇒	=	=	⇒
LAM_{NE}	=	=	=	⇐
LAM_{NMC}	⇐	⇓	=	⇐
LAM_{LCO}	⇐	=	⇓	⇐

curve of the investigated cell. The data for the half-cell potential curves of the cathode and anode are derived from coin cell measurements against Li/Li^+, which were performed after disassembling a pristine cell. For additional information on the preparation of the coin cells, the reader is referred to the experimental Section 4. A detailed mathematical description of the used methodology can be found in Ref. [12]. In order to facilitate comparison, all capacity values are normalized to the extracted capacity of the full cell. The calculated RMSE between the simulated and the measured full-cell voltage curve is 3.7 mV, indicating an excellent fit. The accurate result of the voltage reconstruction in combination with the previously presented simulation of the initial cathode blend mixture ratio, enables simulation of different possible degradation modes (loss of active material on the positive electrode (LAM_{PE}), loss of active material on the negative electrode (LAM_{NE}) and *LLI*) by shifting, stretching, or compressing the corresponding electrode half-cell voltage curves.[28,34] The effects of these simulations on the full-cell voltage and IC characteristics are presented in Figure S1 (Supporting Information). **Table 1** summarizes the changes in IC characteristics (1)–(4) for different separately simulated degradation modes, based on the results from Figure S1 (Supporting Information). This approach requires fitting the initial mixture ratio of the cathode blend, to effectively simulate the separate influence of each blend component ($LAM_{PE,\,NMC}$ and $LAM_{PE,\,LCO}$) on the IC characteristics.[34] In addition, an accurate calculation of the reconstructed full-cell voltage by means of electrode balancing is essential to extract the necessary information on the initial lithium loss (LLI_{ini}) and the lithium reservoir of the cathode, as indicated in Figure 1d. The synthetically generated IC curves are utilized to evaluate the predominant degradation modes observed in the actual measured IC curves over aging. This involves comparing the relative shifts in the real measured IC characteristic over aging against the synthetically generated shifts in the IC curves for separately simulated degradation modes. To our knowledge, this study represents the first application of this methodology to a LTO battery featuring a NMC-LCO blend cathode structure.

The IC curve progression over aging of specimen 1 in continuously pressurized, respectively unpressurized condition is depicted in Figure 1e. Based on qualitative inspection of the IC curves, four distinct degradation areas denoted as characteristics (1), (2), (3), and (4) are identified and labeled in Figure 1e. Table 1 indicates, that due to the stable voltage potential of LTO, the emerging features (2) and (3) are solely attributed to the cathode, enabling effective monitoring of the overall LAM_{PE} by comparing the intensity changes of these features over aging. Specifically, peak (2) at 2.15 V and peak (3) at 2.35 V correspond to the phase transformation of NMC, respectively, LCO, as determined from the prior simulation of the cathode blend characteristic in Figure 1c. For the unpressurized cell in Figure 1e, a clear decrease in peak intensity of the NMC and LCO features is observed, implying the existence of strong $LAM_{PE,\,NMC}$ and $LAM_{PE,\,LCO}$. However, for the cell in pressurized conditions, the decrease in peak intensity within regions (2) and (3) is less pronounced, suggesting a beneficial impact of pressurization on the cathode. Regarding regions (1) and (4), the observed capacity decrease exhibits a similar trend in either pressurized or unpressurized condition. Nevertheless, unlike other IC characteristics, such as (2) and (3), the capacity loss within these regions cannot be solely attributed to a single degradation mode due to the overlapping contributions of *LLI*, LAM_{PE}, and LAM_{NE}. This is evident given the various degradation modes that affect these regions, as shown in Table 1, and requires a more in-depth analysis, provided below by examining the capacity limiting electrode at both the upper and lower cut-off voltages.

Figure 1d reveals that the anode initially limits the amount of extracted capacity in charge and discharge directions, as it restricts the upper and lower cut-off voltage in regions (1) and (4). Therefore, the sharp decrease in the IC feature in region (4) is a distinctive characteristic associated with the LTO anode and any occurring LAM_{NE} immediately results in a visible capacity reduction, which is consistent with the findings from several studies on LTO based LIBs.[28,34] The initial amount of *LLI*, based on the maximum degree of cathode lithiation up to 4.25 V in pristine state, is inferred from Figure 1d to $LLI_{ini} \sim 4\%$. The relatively low amount of LLI_{ini} is in accordance with the intrinsic LTO property of no strong initial surface layer formation, while side reactions at the electrolyte/LTO interface lead to gas generation, resulting in the removal of the outermost lithium-ions.[25] In general, *LLI* does not contribute to the overall capacity loss for LTO-based batteries up to a certain amount, which is explained as follows: Due to the absence of lithium plating risk for LTO batteries as a result of the high anode potential (1.55 V versus Li/Li^+), negative electrode to positive electrode (N/P) ratios below 1 become possible, which is a unique cell design property of LTO-based batteries. The calculated N/P ratio for our investigated cell, based on the presented electrode balancing in Figure 1d, is 0.88 indicating that the cathode effectively offers a lithium reservoir of 12%. Oversizing the cathode enables compensation of any occurring *LLI* by shifting the cathode potential at the upper cut-off voltage toward higher voltages in order to extract more active lithium.[35] This is effectively possible until the cathode potential reaches ≈4.25 V. Beyond that threshold voltage, instead of the anode, the cathode begins to limit the capacity extraction at the upper cut-off voltage and increases the aging rate significantly. Therefore, in case of strong *LLI* over aging the IC characteristic in region (4) is expected to exhibit a rightward shift towards higher voltages, as indicated by Table 1. In addition, once this lithium reservoir is completely utilized the steeply decreasing characteristic in region (4) from the anode diminishes and should instead purely resemble the cathode IC characteristic, as depicted in Figure S1 (Supporting Information). Since in our case, no significant rightward shift toward higher voltages of characteristic (4) is visible and the sharp decrease in the anode feature is still observable for the aged curves IC in Figure 1e, it is concluded that the anode remains the limiting electrode at the upper cut-off voltage

throughout the analyzed aging period. Consequently, the main degradation modes that influence region (4) for our investigated cell are LAM_{NE}, while LLI only has a minor effect on this IC characteristic.

After analyzing region (4) to identify the primary degradation modes affecting the upper cut-off voltage, examination of region (1) allows us to draw conclusions about the limiting electrode at the lower cut-off voltage. The initial limitation of the lower cut-off voltage given by the anode, as depicted in Figure 1d, is maintained as long as the amount of LAM_{PE} is compensated for by the offset between the cathode and anode, i.e., in the early stages of aging LAM_{PE} effectively leads to no visible capacity loss in the full-cell. However, once the offset can not compensate the amount of LAM_{PE} anymore, such that $LAM_{PE}>LLI_{ini} + LLI$, the cathode becomes limiting at the lower cut-off voltage and any further LAM_{PE} leads to an immediately observable capacity loss in the full-cell. Given that, as discussed previously, over aging $LLI<<LAM_{PE}$, implies an early limitation of the lower cut-off voltage by the cathode. This becomes possible because, at sufficiently strong occurring LAM_{PE}, the total amount of available lithium becomes adequate to fully lithiate the cathode upon reaching the lower cut-off voltage. This behavior causes the overall capacity loss to become limited by the cathode at the lower cut-off voltage and by the anode at the upper cut-off voltage, immensely increasing the aging rate. This constellation of limiting electrodes has been theoretically described by Dubarry et al., but to the best of our knowledge, it has never been demonstrated to date.[36]

The occurrence of this electrode limitation configuration is effectively quantifiable by considering the progression of region (1) and comparing it with the expected simulated behavior. The onset of the cathode limitation at the lower cut-off voltage is noticeable by a decrease in the areal capacity of region (1). Figure S2 (Supporting Information) shows the progression of the calculated IC areal capacity of region (1) in pressurized and unpressurized conditions and the simulated trend for up to 20% LAM_{PE}. The comparison shows that the progression of the measured areal capacity in region (1) shows a very similar trend to the expected simulated behavior associated with the cathode-limiting property at the lower cut-off voltage. Hence, it is concluded that during pressurized and unpressurized aging the initial anode limitation of the lower cut-off voltage is replaced by the cathode limiting the lower cut-off voltage. This causes the overall capacity loss to become dependent on the aging behavior of both electrodes, significantly accelerating the overall aging trend.

Given that LAM_{PE} can be immediately quantified based on the progression of IC characteristics (2) and (3) and the condition $LLI<<LAM_{PE}$ holds, LAM_{NE} and LLI are estimated by aligning the simulated IC curve characteristics within region (1) and (4) with the observed IC curves, as demonstrated in Ref. [34]. Figure 1f presents a comparison between the measured and simulated IC curves after 8000 EFC under both pressurized and unpressurized conditions, based on the estimated impact of LAM_{PE}, LAM_{NE} and LLI on the respective IC characteristics. The close alignment between the simulated and measured IC curves supports the validity of the estimated degradation modes. Figure 1g presents the obtained results from the degradation mode analysis for LAM_{PE}, LAM_{NE} and LLI under pressurized and unpressurized conditions. It becomes visible that overall aging is mainly driven by LAM_{PE}. The analysis indicates a significant reduction in LAM_{PE} by applying continuous pressure. More specifically, by comparing the results under unpressurized and pressurized condition, LAM_{PE} is shown to reduce from 17.7% to 9.3%, corresponding to 8.4% reduction of material loss on the cathode. LAM_{NE} exhibited a smaller decrease from 10.6% to 8.3%, yielding to a reduction of material loss by 2.3% on the anode. Additionally, LLI decreased by 1.7% from 4.1% to 2.4%.

2.2. Examination of Main Aging Mechanisms

Post-mortem measurements are conducted on specimen 1 of the cell that was subject to unpressurized cycling. During the prior cycling of specimen 1 under unpressurized condition, a significant volume expansion of the cell volume was observed. **Figure 2**a shows CT scans of the respective cell before disassembling. The cell displayed a relative thickness increase of 7.6% measured in the center of the cell, whereas no significant thickness increase was observed at the edges. The CT scans indicate that the volumetric expansion primarily results from the thickness increase in the jelly-roll, exerting direct pressure against the outer surface of the cell housing. Similarly to the externally perceived change in cell thickness, the most substantial increase in jelly-roll thickness was particularly evident in the center of the cell. These observations serve as a first indication for the existence of gas within the cell.

Optical inspection of the anode material upon cell opening revealed distinct localized round-shaped dark spots at the center of the electrode as well as dark residuals on the lower and upper edges of the electrode, see Figure 2b. Further consideration of Figure 2b shows that the central region of the anode presents a darker shade compared to the lighter-colored upper and lower edges. The separator was easily detached during the disassembly process without notable active material detachment, while a brown stripe within the central region of the separator sheet became visible, matching the darker shade of the center anode portion. These round-shaped black spots are attributed to localized gas pockets and are in accordance with previous studies on LTO batteries, where similar dark spots were identified on the anode and associated with gas generation.[32] It is commonly known that gas generation accompanied by a cell volume expansion poses a significant challenge for LTO-based batteries, especially at elevated temperatures.[25,37,38] Interfacial reactions between the LTO electrode and the surrounding electrolyte solvents are the primary gas-triggering mechanism, despite operating voltages above the reduction potential of common electrolytes.[39–41] Given the elevated ambient temperature of 45°C during our tests, it is reasonable to assume the occurrence of gassing reactions. At an early stage, the aforementioned surface reaction induces gas generation but not to such an extent that it would immediately affect the mechanical cell properties. This is in accordance with the results of Wang et al., which showed an onset of gassing-induced capacity loss for LTO batteries between 900 and 1200 EFC.[42] However, as cycling progresses, the accumulation of distinct and localized gas pockets results in a strong volume expansion of the cell, leading to the mechanical separation of opposing electrodes. The accumulated gas within the cell gradually increases the overall cell volume and should be particularly prominent in the center of the cell due to the stiffness of the housing being highest at

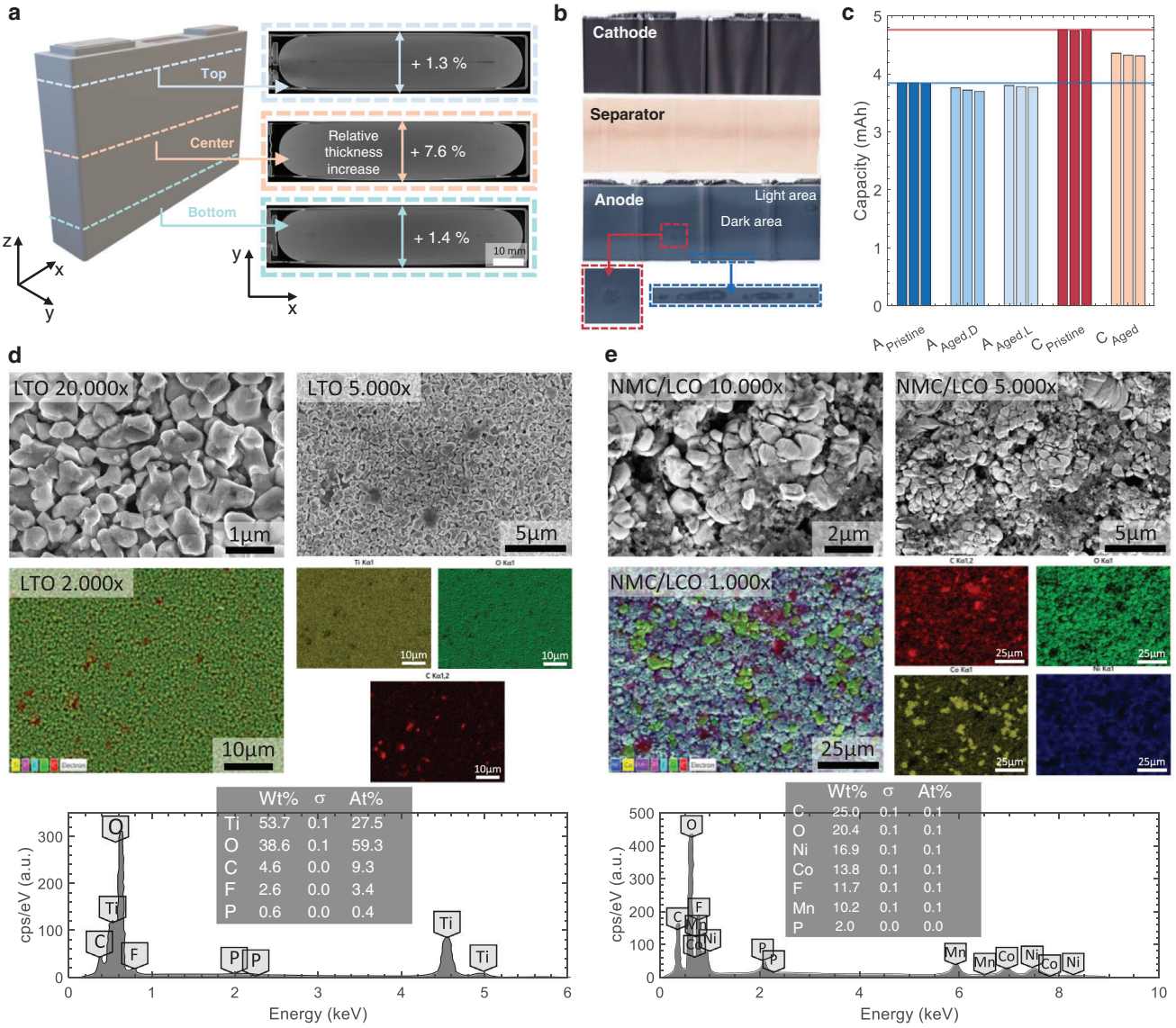

Figure 2. Post-mortem investigation of specimen 1 in unpressurized condition a) CT images comparing the thickness increase of the jelly-roll at the top, center and bottom region. b) Optical investigation of the extracted cathode, separator, and anode material upon cell opening. c) Delithiation capacity of the pristine and aged anode and cathode material measured in half-cell configuration versus Li/Li^+, at room temperature with a current density of 0.09 $mA \cdot cm^{-2}$. d) SEM-EDX analysis performed on aged anode material. e) SEM-EDX analysis performed on aged cathode material.

the edges, which is consistent with the CT images presented in Figure 2a. The presence of gas pockets impacts both electrodes simultaneously, essentially excluding affected electrode portions from the electrochemical reaction due to mechanical separation. Gassing-induced mechanical separation of electrodes has been shown to result in interrupted ionic pathways, increased contact loss, and local displacement of the electrolyte, inevitably causing capacity loss and impedance rise.[29,43] In contrast, the initial optical inspection of the cathode did not reveal any anomalies. However, thickness measurements performed on both electrodes in the pristine and aged state showed that the cathode thickness increased by 16.5%, while no thickness change became visible for the anode, suggesting strong morphological changes in the cathode particles. Although no visible indicators of gas generation were observed on the cathode sheet, the possibility of gas generation, especially at elevated temperatures, cannot be ruled out, considering that the emergence of a developing surface reconstruction layer for NMC cathodes has been associated with gassing.[44,45]

To quantify the extent of electrode-specific material losses, coin cells in half-cell configuration versus Li/Li^+ were built from harvested pristine anode ($A_{Pristine}$) and cathode ($C_{Pristine}$) material. The pristine samples were extracted from the central region of the cell. Furthermore, aged cathode material (C_{Aged}) was extracted and anode material from the light electrode area at the edges ($A_{Aged,\,L}$) and from the dark electrode area in the center ($A_{Aged,\,D}$). The extracted capacity during delithiation of the coin cells is presented in Figure 2c. The extracted capacity showed no signifi-

cant difference between the dark and light electrode areas of the anode. This again indicates that no structural differences exist between the darker and lighter areas of the anode material. The measurements of pristine materials show that the cathode possesses a higher capacity than the anode, which is consistent with the higher energy density of layered oxides compared to LTO. In order to ensure a more consistent comparison, only the extracted cathode capacity between 3.2 and 4.25 V is considered, as any capacity above 4.25 V is not effectively used, as described in Section 2.1. The blue horizontal line in Figure 2c denotes the average capacity extracted during anode delithiation in its pristine state, which is measured at 3.83 mAh. Similarly, the red horizontal line shows the average capacity extracted from the pristine cathode material, measured at 4.75 mAh. The coin cells built from the aged electrode material harvested from specimen 1 under unpressurized condition qualitatively display a similar degradation trend to the one estimated in Section 2.1. The cathode showed an average capacity loss of 9.6%, whereas, in comparison, the anode exhibited less significant aging with only 1.4% capacity loss quantifiable. This confirms the significant cyclic stability of LTO and the comparatively smaller aging impact of LAM_{NE} compared to LAM_{PE} on overall aging, as discussed in Section 2.1.

A notable discrepancy is evident between the previously estimated and measured material losses. In fact, the total capacity loss observed within specimen 1 in Figure 1a under unpressurized condition was 15.9%, which exceeds the combined material losses measured on both electrodes. Furthermore, ICP-OES measurements conducted on aged anode and cathode material did not reveal any significant difference in lithium content compared to pristine material (see Table S1, Supporting Information). Therefore, it is reasonable to attribute the discrepancy between the observed loss in the aged full cell capacity and the material losses from the extracted half-cell material to the presence of gas pockets, which rendered certain electrode regions inactive. However, upon cell opening, the accumulated gas escapes, making previously inactive regions usable again, which no longer affects the extracted capacity of the coin cells. Consequently, gassing appears to be the primary cause of the apparent LAM_{NE}, suggesting that the calculated degradation should be categorized as at least partially reversible.

In order to investigate the surface morphology and distribution of particles and to correlate the observed quantitative capacity loss with morphological and structural changes, SEM-EDX analysis is conducted. Figure 2d,e present the obtained SEM images, as well as the EDX composition analysis for the extracted aged anode, respectively cathode material. In case of the LTO anode, probes were obtained from the dark round-shaped spots and the lighter central area. However, no identifiable differences were observed in terms of surface morphology or material composition between lighter and darker areas (see Figure S3, Supporting Information). This strengthens the hypothesis that the observed round-shaped black spots and the darker-colored center region of the anode are likely a result of the accumulated gas within these areas rather than residuals of a chemical reaction process. The prominence of these darker areas in the center region of the anode aligns with the previously presented results of the CT scans, where stronger volume expansion, coupled with gas generation, was observed in the center region of the cell. The SEM images of the anode in Figure 2d present the results for the probe extracted from the lighter central area (magnified at 5000x and 20 000x). The LTO particles show uniform morphology and even particle distribution, with an average size of 400 nm, while no particle agglomeration is observed, indicating good stability and preservation of the anode structure. Furthermore, the surface of the LTO particles appears intact, with no obvious cracks, fractures, or irregularities. EDX analysis confirmed the presence of oxygen and titanium as dominant elements, with small amounts of fluorine, phosphorus, and carbonate species attributed to the binder and conductive additive. Furthermore, the EDX spectra of the anode did not reveal any traces of cathode metals, indicating the absence of transition metal dissolution from the cathode. In contrast, the cathode in Figure 2e showed significant visual indicators of degradation and structural damage, as observed in the SEM images (magnified at 5000x and 10 000x), although no obvious anomalies were visible in the prior optical investigation of the electrode sheets. The NMC particles notably exhibited cracks, fractures, and compromised surface integrity. Possible explanations for the strong degradation of the cathode could be the high amount of repetitive cycling, resulting in mechanical stress during lithiation and delithiation due to the associated lattice distortion. This can lead to particle cracking and isolate particles, resulting in loss of electrical contact with the electrode surface or current collector.[46–48] Regarding the LCO portion, previous research showed that LCO is highly reactive at elevated temperatures, leading to increased cation mixing, side reactions with organic compounds and the growth of a rock salt-like surface layer, originating from loss of oxygen within the LCO structure.[49–51] This results in irreversible crystallographic changes and thus capacity loss.[52]

In the context of interpreting the physical implications of external pressurization based on the obtained results, pressurization of the cell appears to have a beneficial impact on the two main aging mechanisms identified. Externally applied pressure possibly prevents mechanical separation of the electrodes by reducing the formation of the aforementioned localized gas pockets stemming from LTO side reactions. The applied pressure can compress the generated gas and force it outward the jelly-roll into the unoccupied volume of the cell housing, similar to the results presented by Müller et al.[53]. Additionally, pressurizing the cell potentially has a beneficial impact, particularly on the NMC portion of the cathode, by enhancing particle-to-particle or particle-to-current collector adhesion strength, thus minimizing contact loss resulting from prior particle cracking. In this regard, it should be possible to recover at least some of the identified capacity loss back by pressurizing previously aged cells, which is investigated in the following section.

2.3. Transient External Pressure on Aged Cells

Figure 3a,b depict the recovered capacity under transient applied pressure of 0.3 MPa for previously calendar, respectively, cyclic aged cells dependent on their SOH before pressurization. The solid orange line represents a linear regression model fitted on the investigated data, while the shaded orange area encompasses the 95% confidence interval for the fitted regression line.

Cells subjected solely to calendar aging before pressurization show rather minor capacity variations below 0.5%. Furthermore,

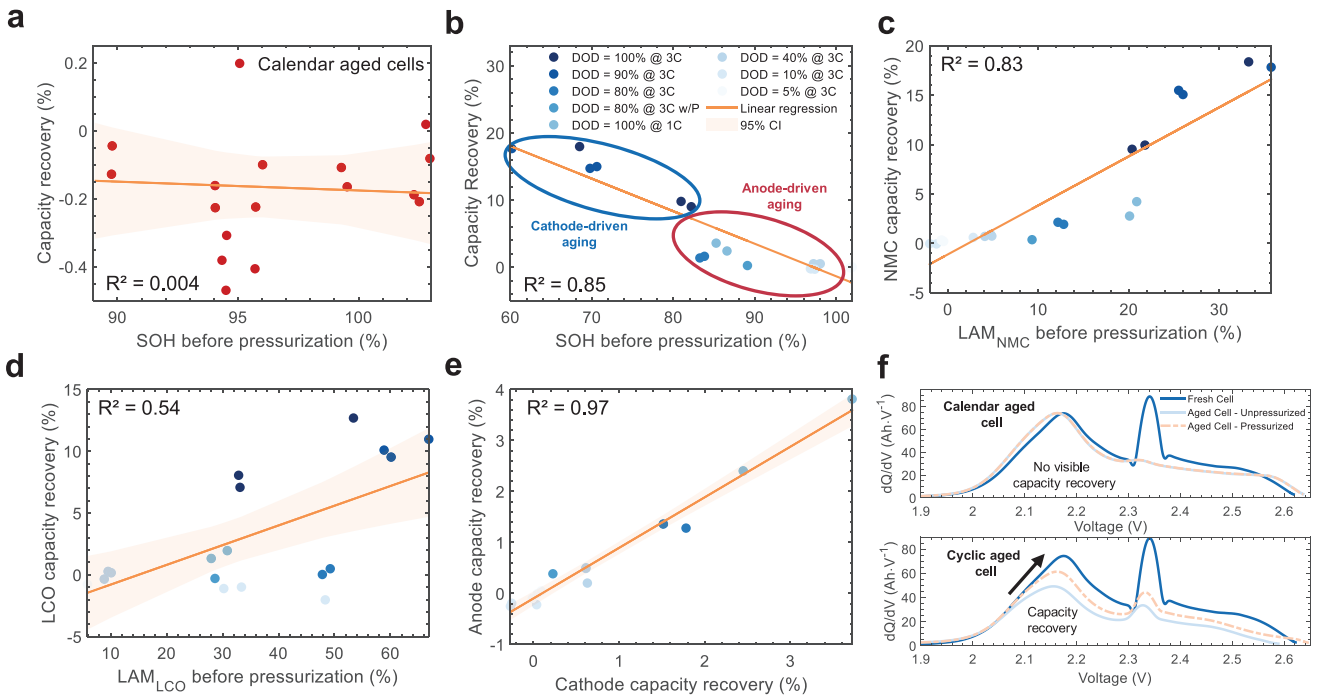

Figure 3. a) Capacity recovery of prior unpressurized calendar aged cells after applying transient pressure plotted over SOH before pressurization. b) Capacity recovery of prior unpressurized cyclic aged cells after applying transient pressure plotted over SOH before pressurization. All cyclic aging tests were previously performed at 45°C. c) NMC capacity recovery after transient pressurization. d) LCO capacity recovery after transient pressurization. e) Comparison of recovered capacity on the cathode and anode for cells with anode-driven aging. f) IC curves in pristine state, unpressurized aged state and aged state with applied transient pressure for a calendar aged cell (90% SOC, 55°C) and a cyclic aged cell (DOD= 90%, 3C, 45°C).

no correlation is found between the amount of recovered capacity and the SOH before pressurization, as $R^2 = 0.004$ indicates no significant dependency between the cell capacity before and after pressurization. Taking measurement uncertainties into account, the overall influence of externally applied pressure on prior unpressurized calendar aged cells is considered rather negligible. Hence, these cells are excluded from further correlation analysis.

However, for the unpressurized cyclic aged cells, significant capacity recovery became visible, revealing a clear trend. The more advanced the prior aging of the cell has progressed, the more capacity can be recovered through external pressurization. This observation is supported by the fact that the six most aged cells during cyclic aging exhibit the largest capacity recovery. The three cells cycled at DOD = 100% with a C-rate of 3C and with SOH values of 68.5%, 80.9%, and 82.2% before pressurization demonstrate a remarkable capacity gain of 17.9%, 9.8%, and 9%, respectively. A similar trend is observed for the three cells cycled with DOD = 90% at 3C. These cells with a previous SOH value of 60.2%, 69.8%, and 70.6% showed a significant capacity recovery of 17.7%, 14.7%, and 15.1%, respectively. All values are related to the initial capacity as per Equation (5). In relative terms, this corresponds to a recovered capacity of up to 57% of the prior lost capacity.

However, cells cycled with DOD = 80% at 3C and DOD = 100% at 1C show a comparatively lower capacity recovery. Furthermore, a reference performance test (RPT) was performed for one of the continuously pressurized cells (DOD = 80% w/P), as presented in Chapter 2.1. This served as a reference to track whether the visible capacity gain could be related to the measurement setup or any other parasitic side effects. However, no capacity gain was observed for this cell, indicating that the observed capacity recovery is in fact purely an effect of external mechanical compression. Cells cycled with lower DODs of 40%, 10%, and 5% at 3C show a rather negligible capacity variation below 1% after applying transient pressure.

The linear regression depicted in Figure 3b shows a strong correlation between the SOH before pressurization and the recovered capacity ($R^2 = 0.85$), suggesting that cells with higher prior degradation during unpressurized cycling recover the most capacity after pressurization. Especially cells cycled at high DODs of above 80% show a significant capacity recovery after applying transient pressure. The pronounced visible effect of pressurization on the capacity characteristic for severely aged cells can be better understood by considering the often proposed two-stage aging mechanism for LTO-based batteries.[28,54,55] As the amount of extracted capacity depends on the electrode that limits the upper and lower cut-off voltages, the actual material losses contribute differently to the overall capacity, as discussed in Section 2.1. As long as the anode limits the extracted capacity in both directions, the observed capacity gain must primarily stem from recovered active material on the anode, e.g., due to the displacement of gas pockets between prior inactivated electrode segments. Therefore, the smaller capacity recovery observed for these specific cells cycled at lower DODs and C-rates is explained by the reduced visible impact of pressurization for cells in which the anode limits the lower and upper cut-off voltages (anode-driven aging). However, for cells cycled at high DODs and C-

rates, the aging of the cathode has progressed so far that the degradation of the cathode begins to limit the extracted capacity, thus determining the overall aging trend with an increased aging gradient (cathode-driven aging). This implies a strong beneficial impact of pressurization on the cathode.

Figure 3c,d depict the calculated capacity recovered in the NMC and LCO portion of the cathode after pressurization. Considering the NMC capacity recovery, a consistent trend becomes visible where cells with prior significant $LAM_{PE,\,NMC}$ exhibit the most notable capacity recovery ($R^2 = 0.83$). This trend is especially notable in cells with cathode-driven aging. Hence, applying transient external pressurization appears to mitigate contact loss stemming from prior particle cracking, thereby leading to an increase in available NMC active material. In contrast, cells where the overall capacity is still limited by the anode capacity show relatively minor capacity recovery. The lower amount of recovered NMC particles for these cells is attributed to lower cyclic stress levels, resulting in a smaller prior active material loss on the cathode. The capacity trend of the LCO portion after pressurization, as presented in Figure 3d, indicates no significant correlation between the amount of recovered LCO capacity and the prior amount of $LAM_{PE,\,LCO}$ ($R^2 = 0.54$). Nevertheless, it becomes visible that for severely aged cells, the capacity loss can be at least partially recovered. However, the recovered amount will not substantially influence the overall cell capacity and is very low compared to the amount of $LAM_{PE,\,LCO}$ before pressurization. Hence, mechanical effects triggered by external pressurization do not substantially influence the LCO portion of the cathode.

Moreover, Figure 3e shows the correlation between the amount of anode and cathode material recovered for cells where aging is still anode-driven. The results indicate a strong positive correlation between the amount of recovered anode and cathode capacity ($R^2 = 0.97$). The similar amounts of recovered capacity indicate that the aging mechanism inhibited by external pressurization affected both electrodes to the same extent. Thus, it is reasonable to attribute the previously observed reversible capacity loss for these cells to ineffective electrode portions separated by gas pockets, which affects both electrodes similarly. Through external pressurization, these segments can be reconnected, aligning with the effect discussed in Section 2.3.

Figure 3f depicts the IC curve progression for a cell subjected to purely calendar aging at 55°C and 90% SOC for 667 days and a cyclic aged cell cycled at 45°C with 3C between 5% and 95% SOC (DOD = 90%). For the calendar aged cell, the IC curves of the pristine unpressurized cell, the aged cell before pressurization and the same aged cell after applying a transient pressure of 0.3 MPa are depicted. After 667 days, the aged cell shows a clear decrease in capacity, indicated by flattening and disappearance of the LCO portion, while the NMC peak shows no significant decrease. The purely observable decrease in capacity within the LCO portion allows an isolated assessment of the impact of mechanical compression on the LCO material component of the cathode. As expected, there is no identifiable deviation between the aged IC curve subjected to transient pressure and the unpressurized aged IC curve. This further implies that externally applied pressure, in this case, does not have a significant beneficial effect on the LCO portion of the cathode.

Considering the cyclic aged cell, a visible decrease in the NMC and LCO portions is observed for the aged cell prior to pressurization. However, in contrast to the calendar-aged cell, we can clearly identify an increase in the IC curve characteristics when transient pressure is applied. This increase becomes apparent for the NMC portion as well as for the LCO portion, resulting in an increased amount of available extracted capacity. These observations emphasize previous observations of a stronger beneficial effect on the NMC portion of the cathode by pressurization. Concerning the LCO portion, we can observe an increase in the characteristic of the IC curve for cyclic-aged cells, which was not evident for the calendar-aged cell. Here, it is important to remember that the IC characteristic of the NMC portion influences the peak height of the LCO portion, as depicted in Figure 2c. However, as presented in Figure 3d, there is indeed a small capacity gain observable stemming from the LCO portion. This disparity could be attributed to varying distinct causes of aging during calendar and cyclic aging, affecting the LCO material differently. In the case of the pure calendar-aged cell in Figure 3f, pressurizing the cell will not yield any substantial capacity recovery due to exclusive prior oxygen depletion. However, considering cyclic aged cells in addition to the thermally induced aging causes described above, gradual degradation during cycling due to an increased uneven lithium distribution at the particle level can cause morphological defects, such as additional loss of contact.[56] Nevertheless, the impact of both effects on overall capacity appears to be minor compared to the effect of reduced contact loss on the NMC portion.

Figure 4a presents the corresponding impedance spectra for the cyclic aged cell presented in Figure 3f before pressurization, depicted in a Nyquist graph. The intersection between the x-axis and the impedance spectra at high frequencies (6000–500 Hz) shifts toward lower values with increasing SOC, indicating a decrease in ohmic resistance with higher SOCs. This behavior is attributed to the spinel-rock salt phase of LTO, which results in higher electronic conductivity at higher degrees of lithiation of LTO.[27] Furthermore, NMC is known to exhibit increased electronic conductivity with decreased lithium content.[57] Given that high full-cell SOCs correspond to high lithiation states for the anode and low lithiation states for the cathode, both electrodes display enhanced electronic conductivity properties, resulting in an overall decrease in ohmic resistance.

The width of the semi-arc observed at mid frequencies (500–10 Hz) reflects the impeded charge transfer process between the electrolyte/electrode interface. In general, the charge transfer characteristic of LTO batteries, particularly for cyclic-aged cells, is predominantly affected by the cathode due to limited surface film formation on the anode.[44,58] This is in accordance with the previously presented post-mortem measurements in Section 2.1, where no prominent surface layer formation was observed for the anode, whereas significant structural damage and a thickness increase became visible for the cathode. Considering the progression of the charge transfer semi-arc for the investigated unpressurized cells reveals an increase at very high and very low SOCs, resembling the charge transfer behavior of pure NMC.[59]

The solid-state diffusion branch, observable at low frequencies (10–0.01 Hz), exhibits a steeper slope at high SOCs, indicating impeded lithium diffusion characteristics within this range. However, a notable decrease in the steepness of the diffusion branch becomes apparent for low SOCs. This change is likely attributed to the sluggish lithium diffusion behavior within the

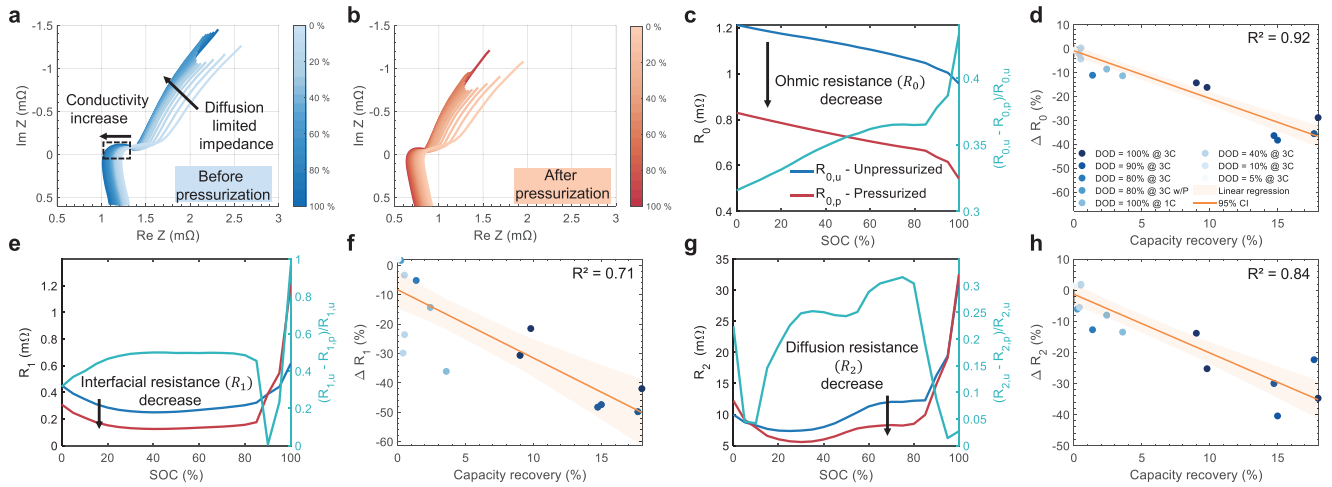

Figure 4. a) Impedance data obtained from EIS measurements performed on a prior unpressurized cyclic aged cell (DOD = 90%, 3C, 45°C) between SOC = 0–100% and 6000–0.01 Hz frequency range depicted in a Nyquist plot. b) Impedance data obtained from EIS measurements performed on the same cyclic aged cell as presented in a) with transient pressure applied c) R_0 over SOC before and after pressurization. d) Relative change of R_0 at SOC = 50% for all prior unpressurized cyclic aged cells. e) R_1 over SOC before and after pressurization. f) Relative change of R_1 at SOC = 50% for all prior unpressurized cyclic aged cells. g) R_2 over SOC before and after pressurization. h) Relative change of R_2 at SOC = 50% for all prior unpressurized cyclic aged cells.

LTO rock-salt phase, known to be approximately one order of magnitude smaller than in the spinel phase.[60] Furthermore, for LTO the chemical diffusion process is proposed to transition from an electronic to an ionic limited diffusion process depending on the lithiation state of the LTO material.[61] In contrast, for NMC, the chemical diffusion process is reported to be always limited by lithium-ion transport, given the more than 10^7 times lower ion diffusivity compared to the electronic conductivity.[57] However, prior research found the lithium-ion diffusion coefficient of NMC between 3.9 and 4.4 V to be three to two orders of magnitudes higher than the reported LTO diffusion coefficient in the lithium-rich rock-salt phase.[57,59] Hence, the particularly sharp increase in the diffusion branch at high SOCs is attributed to the low diffusion coefficient of LTO at high lithiation states.

Figure 4b depicts the results of the EIS measurements for the same cell under applied transient pressurization of 0.3 MPa. Notably, the ohmic resistance decreases significantly, indicated by a leftward shift of the intersection between the x-axis and the impedance spectra at high frequencies. Additionally, the charge transfer semi-arc becomes smaller, and the slope of the solid-state diffusion branch steepens. These observations suggest facilitated charge transfer at the electrode/electrolyte interface and enhanced lithium diffusion kinetics due to applied external pressurization.

In order to quantitatively assess the qualitative observations made previously, the kinetic processes within the cell are modeled using an equivalent circuit model (ECM) that is fitted to the measured EIS data.

In Figure 4c,e,g the fitted ECM parameters for the prior cyclic aged cell in unpressurized condition (blue), pressurized condition (red) and the relative change compared to the unpressurized value (turquoise) are presented throughout the measured SOC range. The ohmic resistance R_0 shows a linear decline as SOC increases, up to SOC = 95%, where a sharp drop in resistance can be observed. Furthermore, it becomes visible that the ohmic resistance decreases significantly after external pressure is applied. Analyzing the relative change of R_0 indicates that the effect of pressurization on the ohmic resistance is notably amplified, especially at high levels of SOC. This trend corresponds to the previously mentioned spinel-rock salt phase transformation of LTO and the enhanced electronic conductivity of NMC upon delithiation. The ohmic resistance is primarily influenced by the ionic resistance of the electrolyte and the contact resistance between the active material and the current collectors.[62] Hence, the obtained results suggest that the application of external transient pressurization facilitates the movement of lithium-ions within the electrolyte and electron transfer. This is likely due to the reduced porosity of the separator and increased contact between the current collector and cracked active material, especially from the NMC portion.

The charge transfer resistance R_1 in Figure 4e shows a U-shaped pattern with a minimum at 50% SOC. This pattern is consistent with the SOC dependent charge transfer characteristic of NMC, which demonstrates a U-shaped curvature as reported in Ref. [59]. A notable decrease in charge transfer resistance R_1 is observed after applying external pressurization. The reduction of R_1 by external pressure is attributed to the improved electrode/electrolyte contact. This improvement results in better charge transfer, which was previously hindered by contact loss on the cathode and the presence of localized gas pockets.

The diffusion process, represented by R_2 in Figure 4g, exhibits a U-shape trend similar to the charge transfer resistance, with a notable increase between SOC = 90-100%, indicating the onset of diffusion-limiting properties from the LTO rock-salt structure. The visible decrease of R_2 due to short-term pressurization suggests improved diffusion properties between SOC = 10–90%. However, considering the relative change of R_2 reveals that the effect of external compression on the diffusion characteristic is significantly reduced at high and low SOCs. Hence, diffusion remains impeded at these points due to the inherent diffusion-

limiting nature of LTO. However, in general, external pressurization appears to be beneficial for the diffusion properties, indicating improved mass transport as a result of shortened diffusion pathways. Furthermore, enhanced electrolyte penetration into previously inaccessible electrode areas due to external mechanical compression can be expected, further promoting diffusion.

Figure 4d,f,h illustrates the relative change of the ECM parameters R_0, R_1 and R_2 at 50% SOC before and after transient pressurization for prior unpressurized cyclic aged cells plotted against the amount of recovered capacity. The solid orange line represents a linear regression model fitted to the data, while the shaded area indicates the 95% confidence interval for the fitted regression line. The relative change in ohmic resistance R_0 as depicted in Figure 4d displays a significant decreasing trend after transient pressure is applied. It becomes evident that cells exhibiting increased capacity recovery also demonstrate a notable decrease in R_0. Specifically, cells cycled at high DODs show a decrease of R_0 by up to 38.3%. Consequently, cells cycled at lower DODs of 5%, 10%, and 40% exhibit a minor decrease in R_0 below 5% when transient pressure is applied. The strong correlation observed between the ohmic resistance and the amount of recovered capacity ($R^2 = 0.92$) suggests that the decrease of ohmic resistance by external pressurization is primarily a result of counteracting the same aging mechanism across all investigated cells, namely minimizing contact loss due to prior particle cracking. Another observation is the decrease in ohmic resistance for cyclic-aged cells with DOD = 100% at 1C and DOD = 80% at 3C. Despite the lower amount of recovered capacity compared to cells cycled at DODs of 100% and 90%, a significant decrease of R_0 becomes visible.

This effect is amplified when investigating the relative change in charge transfer resistance R_1 as depicted in Figure 4f. A substantial decrease in charge transfer resistance is observed even for cells cycled at low DODs. Despite this significant decrease in R_1, only a minor capacity recovery became effectively visible for these cells. Thus, a significant beneficial impact of pressurization on the charge transfer characteristic becomes evident, although no strong degradation of the cathode is expected at lower stress levels. This indicates that during pressurization, charge transfer for these cells is not primarily influenced by the amount of recovered capacity as observed for R_0. Instead, mechanical separation due to substantial gas generation, even at low DODs, is expected to result in local displacement of electrolyte, forming a barrier layer between active material particles and the electrolyte.[30] This inevitably results in an increase in the charge transfer resistance. Hence, even though the beneficial impact of pressurization is rather hidden in terms of capacity recovery due to the anode limiting capacity property, a significant enhancement of the impedance characteristics can be expected. Cells cycled at high DODs exhibit the most substantial decrease in charge transfer resistance of up to 49.8%. The comparably low correlation of $R^2 = 0.71$ between the change in R_1 and the recovered capacity supports the assumption of two distinct suppressed aging mechanisms by transient applied pressure influencing cells at different aging stages to varying degrees.

Considering R_2 in Figure 4h reveals a similar significant decrease for cells that were previously cycled at high DODs. Specifically, cells cycled at high DODs exhibited a decrease in R_2 by up to 40.5%. Similar to the charge transfer resistance, significant changes in R_2 are also observed for cells cycled at lower stress levels. This further indicates the impeding effect of both identified main aging mechanisms, namely particle cracking from the cathode and gassing, on the diffusion process, which is enhanced by transient applied pressure. Furthermore, enhanced electrolyte penetration into previously inaccessible electrode areas due to external mechanical compression is expected. Another particularly interesting observation is the decrease in R_2 for the investigated cell cycled under continuous pressure by 6.1%. Unlike R_0 and R_1, where no significant decrease was visible for this particular cell, the immediate decrease of R_2 is attributed to shorter diffusion pathways, becoming effective immediately after pressure is applied.

Table 2. Overview of the first cycling regime in unpressurized condition.

Specimen	C-rate	Temperature [°C]	SOC range [%]	DOD [%]	EFC [%]
A1	3C	45	0–100	100	2400
A2	3C	45	0–100	100	3600
A3	3C	45	0–100	100	2800
B1	3C	45	5–95	90	7600
B2	3C	45	5–95	90	7600
B3	3C	45	5–95	90	7600

2.4. Continuous External Pressure on Aged Cells

The six cells most affected by transient pressurization, as presented in Section 2.3, in terms of capacity recovery, are further cycled under continuously applied pressure, similar to the cells in Section 2.1. The transition from unpressurized cycling to initial bracing and further continuous cycling is done in order to analyze the longevity of the observed capacity recovery.

The highest capacity recovery became visible for each set of three cells cycled at high DODs of 100% (specimen A1, A2, and A3), respectively 90% DOD (specimen B1, B2, B3), since higher DODs correlate with stronger occurring LAM_{PE}. The following second round of cycling with continuously applied pressure was then performed under different conditions. **Tables 2** and **3** give an overview of the first, respectively, second cycling regimes in unpressurized and pressurized conditions.

One cell from each set (specimen A1 and B1) was selected and cycled for an additional 3600 EFC with DOD = 80% between 10% and 90% SOC at 25°C. The progression of the capacity curve for these two cells is depicted in **Figure 5a**. During initial unpressurized cycling, a large variance in the capacity fading trend be-

Table 3. Overview of the second cycling regime in pressurized condition.

Specimen	C-rate	Temperature [°C]	SOC range [%]	DOD [%]	EFC [%]
A1	3C	25	10–90	80	3600
A2	3C	25	0–100	100	3600
A3	3C	45	0–100	100	3600
B1	3C	25	10–90	80	3600
B2	3C	35	0–100	100	3600
B3	3C	35	0–100	100	3600

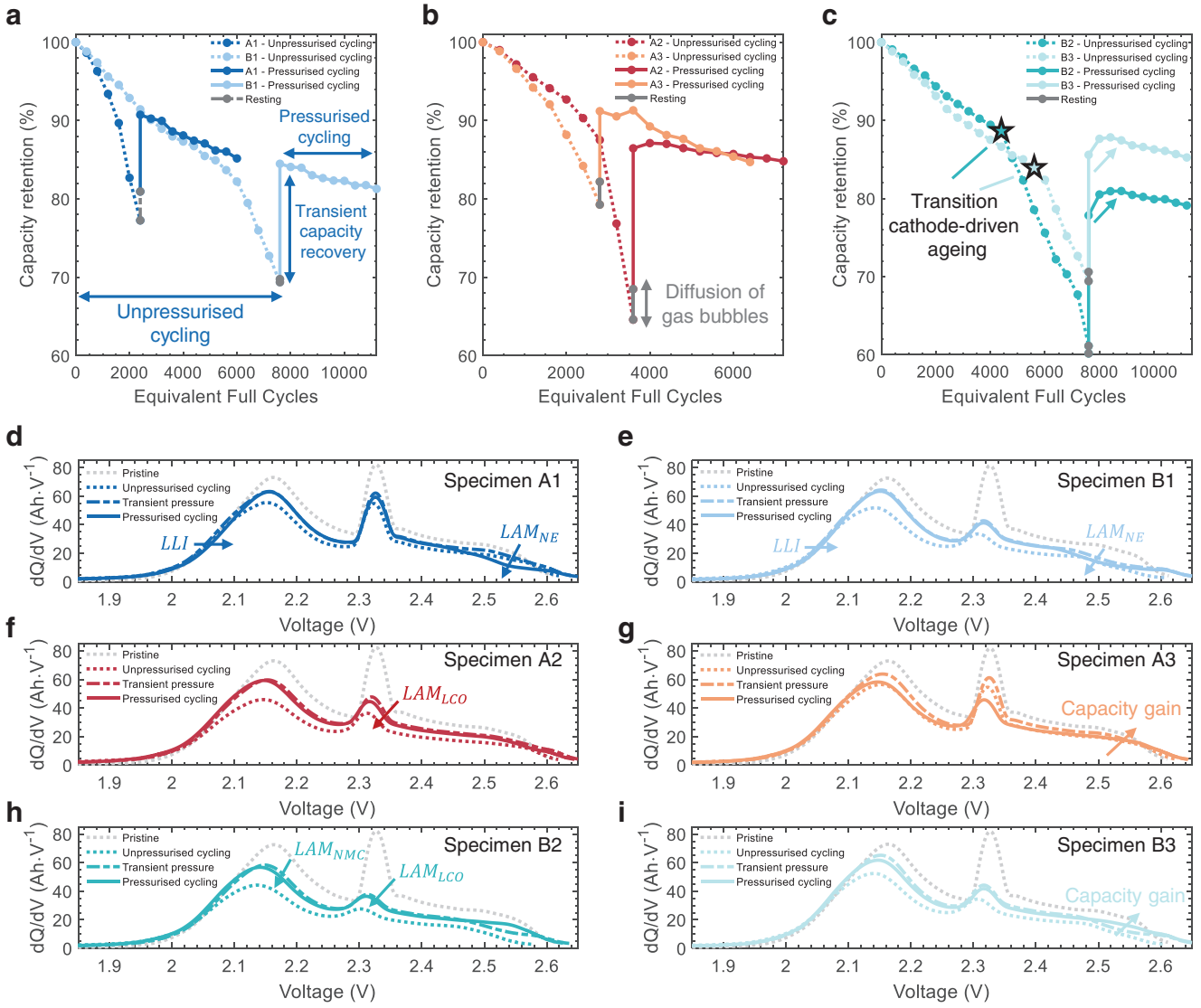

Figure 5. a) Capacity progression over EFC for prior unpressurized cycling followed by a resting phase and further continuous pressurized cycling for specimen A1 and B1 b) specimen A2 and A3 and c) specimen B2 and B3. d) IC curve progression in pristine state, after initial unpressurized cycling, after application of transient pressure and continued further cycling with external pressure for specimen A1 e) specimen B1 f) specimen A2 g) specimen A3 h) specimen B2, and i) specimen B3.

tween both cells is identifiable due to different investigated cycle depths. Furthermore, specimen A1 showed a significant volume expansion during initial unpressurized cycling due to strong gas generation, which was triggered by the high ambient temperature of 45°C in combination with increased cycle depths. Hence, after only 2400 EFC, the cell showed a substantial capacity reduction of 22.73%. After a resting period, the inflation decreased and the cell experienced a partial capacity recovery of 3.68%. This is assumed to be due to the diffusion of gas bubbles into unoccupied spaces of the cell housing reconnecting previously separated electrode compartments, in accordance with Section 2.1. Specimen B1 showed a capacity decrease of 30.63% after 7600 EFC of unpressurized cycling. However, there were no apparent external indicators of an increased amount of gas generation, and thus no noticeable capacity recovery was visible after the resting period. Furthermore, the aging gradient for this cell increased drastically after 5600 EFC, indicating the transition from anode-dominant degradation behavior to a more pronounced cathode-driven aging trend. The following marked increase in capacity, visible for both investigated cells, resulted from the external transient pressurization initially applied, as explained in Section 2.3. Specimen A1 showed a pressure-induced capacity recovery of 9.8%, while specimen B1 showed a capacity increase of 14.7%. However, upon adjusting the operating conditions for both cells and continuing cycling with externally applied pressure, specimen A1 experienced a capacity decrease of 5.6%, while the capacity of specimen B1 decreased by 3.2% after 3600 EFC. The results show that the aging rate decreased drastically when continuous pressure was applied in a second cycling round. The capacity retention exhibited consistent and stable behavior, appearing to be

superior compared to the observed aging behavior during previous unpressurized cycling.

The remaining two cells from set A, specimen A2 and A3, underwent cycling under continuous pressure with the same DOD = 100% but at different ambient temperatures to investigate the temperature dependency of aging under continuous pressurization. The capacity progression of specimens A2 and A3 is depicted in Figure 5b. In this case, the capacity for both cells exhibited a rapid decline during initial unpressurized cycling due to the high DOD resulting in strong LAM_{PE}, similar to specimen A1. The capacity loss amounted to 35.4% (specimen A2), respectively 20.7% (specimen A3) and showed a high variance, although the cells were cycled under the same operation condition. Similar to specimen A1, the cells experienced a substantial volume expansion, attributed to gassing effects. After a resting period, there was an observable partial capacity recovery of 3.9% for specimen B2 and 2.9% for specimen A3. The application of transient pressure resulted in a capacity increase of 17.9% (specimen A2), respectively 9% (specimen A3). Further cycling under continuous pressure led to a minor capacity reduction of 1.6% for specimen A2, whereas specimen A3 showed a capacity reduction of 6.5% due to the higher ambient temperature of 45°C. This observation highlights the strong impact of ambient temperature on capacity retention during continuous pressurized cycling.

The remaining two cells of set B, specimen B2 and B3, were cycled with a DOD of 100% at a reduced ambient temperature of 35°C. The progression of the capacity is illustrated in Figure 5c. Initially, during the previous unpressurized cycling, both cells exhibited a small variance in the capacity fading trend. However, after 4400 EFC, specimen B2 transitioned into the cathode-driven aging stage, in which the cathode degradation became the limiting factor for the aging gradient, while specimen B3 entered this stage after 6000 EFC. Both cells exhibited a substantial capacity reduction after 7600 EFC of 39.8%, respectively 30.6%. The following resting phase did not lead to significant capacity recovery. However, after applying transient pressure, the investigated cells showed a pressure-induced capacity recovery of 16.7% (specimen B2) and 15.1% (specimen B3). Interestingly, the following cycling under continuous external pressurization initially led to an additional capacity gain of 3.1% (specimen B2), respectively, 2.2% (specimen B3) after 800 EFC. The remaining 2800 EFC resulted in a capacity loss of 1.8% (specimen B2), respectively, 2.6% (specimen B3). This is particularly interesting considering two observed trends. First, the aging gradient during cycling under continuous pressure is reduced compared to the unpressurized cycling round, although a higher DOD is used. Second, the capacity loss of specimen B2 and B3 is lower compared to the capacity loss of specimen B1 during continuous pressurized cycling, although B2 and B3 were cycled at a higher DOD and ambient temperature.

Figure 5d,e depicts the IC curve progression of specimen A1 and B1 in pristine state, after the initial unpressurized cycling round, after the application of transient pressure and continued cycling with external pressure. During initial unpressurized cycling, both investigated cells show significant degradation compared to the pristine state. This is reflected in a decrease in the NMC and LCO portions in the respective IC curves, whereas a much stronger degradation for the cell extracted from set B is observable, as it was subject to a higher number of EFCs. The following transient pressurization led to an immediate notable increase in capacity. The LCO portions of the respective IC curves after pressurization vary due to different initial aging conditions. Notably, no significant effect of pressurization on the LCO portion of the cathode is expected, according to the results of Section 2.3. Hence, the observed increase in the IC characteristic can be primarily attributed to the overlapping portion of the NMC capacity within the LCO voltage region. However, the NMC portion for both cells demonstrated a capacity recovery to a similar extent. Further continuously pressurized cycling for the investigated cells resulted in only a minor decrease of the NMC and LCO peaks at 2.15 V, respectively 2.35 V, indicating mitigation of LAM_{PE}. Furthermore, the NMC characteristic undergoes a rightward shift toward higher voltages, with a more pronounced shift observed in specimen B1 compared to specimen A1. As discussed in Section 2.1, this distinctive shift strongly suggests the presence of *LLI*. In the voltage region of 2.45–2.6 V, the IC curve characteristic exhibits the strongest decrease. The capacity reduction in this region can only stem from LAM_{NE}, which is consistent with the minor influence of LAM_{PE} and *LLI* under pressurized conditions. Hence, we can conclude that during continuously pressurized cycling, the capacity degradation is predominantly influenced by LAM_{NE} with only a partial contribution of *LLI*. In comparison to prior unpressurized cycling, the aging rate of LAM_{PE} is significantly reduced when external pressure is applied. This improvement is primarily attributed to enhanced particle/particle or particle/current collector contact on the cathode, consequently inhibiting further occurring LAM_{PE}. The amount of pressure-induced recovered capacity appears to have resulted in a back-transitioning into the first aging stage, where the overall capacity degradation becomes again solely dependent on the aging of the anode, which inherently offers better cyclic stability and thus reduces the aging gradient.

Figure 5f,g presents the corresponding IC curves for specimen A2 and A3. It becomes visible that prior unpressurized cycling resulted in substantial degradation of the NMC and LCO portion, which is partially recovered after applying transient pressure to the cell. However, extended continuous cycling at 25°C for specimen A2 did not yield any significant capacity reduction despite an increased DOD. The NMC portion of the respective IC curve remains unchanged, while a minor decrease is observed in the LCO portion. In contrast, specimen A3 cycled at 45°C exhibits a more pronounced capacity loss, especially from the LCO portion of the cathode. This again shows the high proneness of LCO to increased temperatures. The results highlight the strong temperature dependency of the occurring aging mechanisms. Despite the fact that specimen A2 showed a higher capacity fade during prior unpressurized aging, the capacity fade during continuous pressurized cycling of specimen A3 surpassed that of specimen A2. This leads to the finding that high ambient temperatures remain a critical stress factor, even when cycling is performed under continuous pressure.

The corresponding IC curves for specimen B2 and B3 are depicted in Figure 5h,i. Again, strong degradation of NMC and LCO becomes visible during unpressurized cycling, which is partially recovered after applying transient pressure to the cell. Further continuous cycling resulted in a minor capacity loss on the

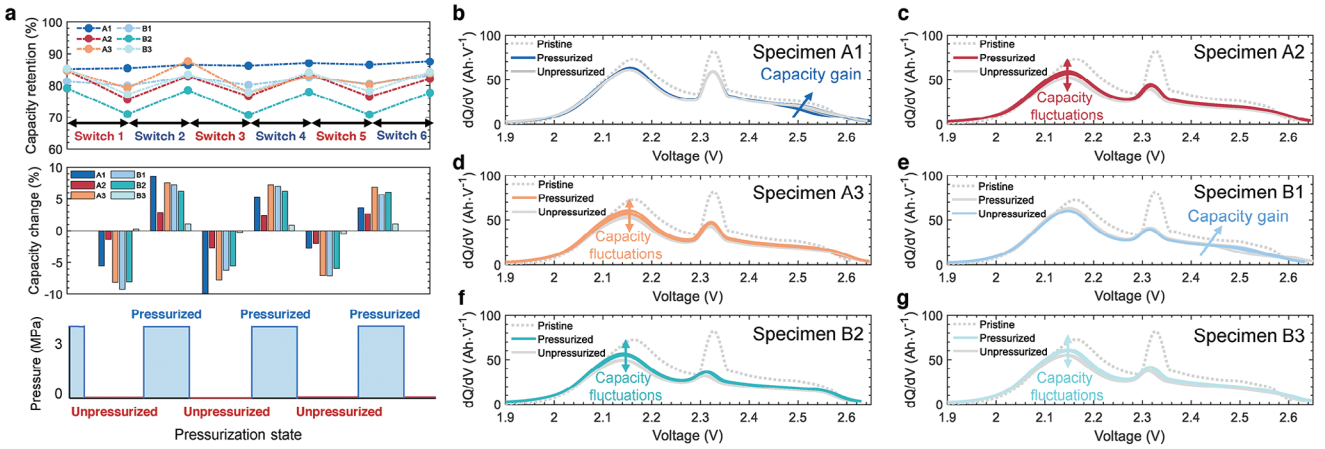

Figure 6. a) Capacity retention, relative change in capacity and corresponding pressurization states for all specimens in sets A and B during intermittent applied pressure. b) IC curve progression in pristine state and during intermittent applied pressure for specimen A1 c) specimen A2 d) specimen A3 e) specimen B1 f) specimen B2, and g) specimen B3.

NMC and LCO portion, which was more pronounced for specimen B3. Furthermore, an increase was observed in the voltage region between 2.45 and 2.6 V, which was also reflected in an increase in the capacity progression (see Figure 5c). This increase was initially not visible during transient pressurization and indicates that cycling at higher DODs under continuous pressure resulted in this capacity gain. The long-term cycling of LTO has been demonstrated to induce structural disordering due to trapped lithium remaining within the LTO structure, resulting in diminishing ionic and electronic conductivity properties.[63] The following capacity increase observed in the IC curve characteristic may be attributed to the adapted cycle SOC region, leading to higher delithiation states in the LTO material compared to the prior cycling condition. In this specific case, prior unpressurized cycling was performed with 90% DOD between 5% and 95% SOC. Hence, performing repetitive pressurized cycling between 0% and 100% SOC possibly triggered this permanent capacity gain, stemming from more available lithium due to higher delithiation states of the LTO anode.

2.5. Intermittent Transient Pressure on Aged Cells

The six cells cycled under continuous pressure, as presented in Section 2.4, are further subject to intermittent transient pressure to determine whether the observed capacity recovery could be maintained without the need for continuous pressurization.

Figure 6a illustrates the capacity retention, the relative change in capacity and the corresponding pressurization states for all specimens in sets A and B. Intermittent pressure is applied to cells by successively applying and withdrawing pressure after continuous pressurized cycling as described in Section 2.4. Each data point in the upper graph represents the capacity retention after performing a RPT in the respective pressurization state. The middle graph in Figure 6a shows the capacity variation associated with each transition of the pressurization state, while the lower graph schematically represents the respective pressurization state.

For specimen A1, the extracted capacity in the pressurized state increased by 2.4% from initially 85.2% to 87.6% after six pressure mode switches (switch 1 to switch 6). The extracted capacity of specimen B1 increased under pressurized conditions by 1.87% from 81.29% to 83.16%, while no significant capacity increase was visible under unpressurized conditions after four pressure mode switches (switch 2 to switch 5) for both cells. The relative capacity variation of specimen A1 during intermittent applied pressure shows a relatively constant capacity behavior, with only minor fluctuations in the range of –0.55 to 1.06%. However, the capacity variations for specimen B1 showed larger fluctuations, in the range of –2.68 to 2.88%. In both cases, the extracted capacity increased when the cell was in a pressurized state, while a capacity decay became visible in an unpressurized state. The average change in capacity per pressure mode switch was 0.4% for specimen A1, respectively 0.3% for specimen B1, indicating that successively applying transient pressure averages into a capacity increase of 0.3%, respectively 0.4% per pressurization switch.

The extracted capacities of specimens A2, A3, B2, and B3 after six successive switches of the pressurization state show larger fluctuations compared to specimens A1 and B1 of up to 10% per pressurization switch. For these cells, the extracted capacity in pressurized state decreased after six pressure mode switches by 2.7%, 0.8%, 1.3%, and 1.1%, respectively. Similar to specimen A1 and B1, the capacity change in unpressurized condition from switch 2 to switch 5 did not change significantly over the course of the measurement (< 1%). Furthermore, the average capacity variations for all six pressurization switches were, respectively, –0.45%, –0.14%, –0.24%, and –0.17% per switch, indicating that on average for each specimen capacity is irreversibly lost during intermittent pressurization.

Figure 6b–g shows the IC curve progression for each specimen at each pressurization state. The dotted gray line indicates the behavior of the initial IC curve for the respective cell. It becomes visible that for specimens A1 and B1 no significant change in either pressurized or unpressurized state is visible for the LCO portion of the cathode, again indicating that external pressurization has no significant influence on the LCO portion

as described in Section 2.3. Additionally, for the NMC portion of the cathode, the IC curves indicate that the capacity increases slightly in the pressurized state while it decreases in the unpressurized state, aligning with the previously presented capacity results. The IC characteristic in the region of 2.45–2.6 V shows an increase after the first switch from a pressurized to an unpressurized state. However, the subsequent pressurization switches did not result in significant changes in this IC characteristic. A similar increase was observed within this region for continuous pressurized cycled cells in Section 2.4. As described in the previous section, long-term cycling of LTO could have resulted in lattice distortion by trapped lithium remaining in the LTO structure. Hence, the repetitive cycling performed between 0 and 100% SOC from the RPTs possibly triggered this permanent capacity gain.

All other presented IC curves indicate a clear trend. The application of intermittent pressure leads to a significant increase in the NMC portion, while withdrawing pressure decreases the NMC peak. Additionally, there is a decrease in the visible LCO peak originating from the superposed NMC capacity within this voltage region. The results indicate that pressurization results in recovered contact of cracked NMC particles, thus resulting in a capacity increase. However, upon withdrawing the pressure, the reestablished contact of the NMC particles is lost again, leading to a drop in capacity. Taking into account that specimens A2, A3, B2, and B3 have been prior continuously pressurized cycled at higher DODs of 100%, suggests that higher DODs translated into stronger occurring LAM_{PE}. Hence, more active material is recovered when pressure is applied, while at the same time, withdrawing pressure results in a more severe capacity drop compared to specimens A1 and B1. Nevertheless, for specimens A1 and B1, successively changing the pressurization state from pressurized to unpressurized could result in a long-term increase in usable capacity.

3. Conclusion

This study examined the impact of various external pressurization modes on pristine and aged LTO batteries. Our results indicate that continuously applied pressure on pristine cells during cycling leads to a 42% reduction in capacity loss compared to unpressurized cells under otherwise similar operating conditions. The predominant degradation mode observed under both pressurized and unpressurized conditions was LAM_{PE}, which was significantly reduced by 8.4% under applied pressure. Post-mortem analyses verified that overall aging is mainly driven by the cathode and revealed two main aging mechanisms for unpressurized cyclic aged cells. First, extensive cycling induced particle cracking on the cathode, particularly affecting the NMC portion. Second, an inspection of the anode electrode material revealed distinct localized dark spots, which were attributed to gas pockets generated at high ambient temperatures, causing mechanical separation of certain electrode regions.

Our findings demonstrate that the use of external pressure can mitigate the two primary aging mechanisms identified. Transient pressure applied to already aged cells demonstrated a notable capacity recovery of up to 57% of the previously lost capacity depending on the limiting electrode configuration and the specific prior aging pathway. For anode-driven aging, applying pressure can expel gas bubbles and reconnect previously separated electrode segments, whereas for cathode-driven aging in addition, NMC active material particles are reattached, counteracting previously observed particle cracking. However, no significant changes were observed for the LCO portion of the cathode upon pressurization, which is attributed to irreversible crystallographic changes, which remain unaffected by external mechanical compression. A correlation analysis performed with various parameters indicated that a significant capacity recovery and impedance decrease is associated with extensive prior aging of the respective cells. EIS measurements indicated that reduction in ohmic resistance can be largely attributed to the reattachment of NMC particles. The decrease in charge transfer resistance was related to the reconnection of previously separated electrode segments, which became significantly visible even for cells with only minimal capacity recovery.

Continuous pressure applied to prior unpressurized cyclic aged cells demonstrated enhanced cyclic stability, primarily due to improved contact of NMC particles on the cathode, inhibiting further LAM_{PE}. As LAM_{NE} becomes the predominant aging mode under these conditions, the anode inherently offers better cyclic stability, thus reducing the aging gradient. Intermittent pressure showed the ability to increase the capacity even after pressure removal, depending on the prior aging of the cell. However, significant fluctuations were observed and the capacity gain upon pressure removal could not be sustained.

This work adds value to both first- and second-life applications of battery systems by shedding light on distinct aging and healing mechanisms in LTO batteries, their dependence on external pressure and their interaction. Understanding these mechanisms is essential for designing strategies in first-life applications to mitigate degradation and enhance battery pack performance and lifetime. Furthermore, the investigated pressure-induced capacity recovery holds significant promise for second-life applications.

4. Experimental Section

Pressurization Setup: The bracing setup consists of three aluminum plates and a pressure sensor. The pressure sensor was placed in the middle between the two upper aluminium plates so that the mechanical load can be measured and set to be applied uniformly along the surface of the cell. The cell was placed between the lower of the two upper aluminum plates and an additional third aluminum plate at the bottom, as depicted in **Figure 7**. The three plates were held together with nuts and bolts. The nuts were screwed so that the set moment on each nut was 2 Nm, resulting in an applied pressure of ≈0.3 MPa on the cell. The pressurization method is the same for all presented pressurized cells.

Reference Performance Test: RPTs were performed using a Digatron MCT ME. The channels offer accuracies of 0.1% over the full scale. All characterization tests were performed after the cell was cooled to 25 ° C within a MK53 binder. Before each characterization test, the cells were CCCV charged with a C-rate of 1C until the upper cut-off voltage was reached and the floating current was below C/20. Afterward, a 30-min rest period was applied. Then, two consecutive capacity tests were performed, consisting of a CC discharge with C/3 followed by a resting period of 30 min and a CCCV phase in charge direction with 1C until the float current was below C/20. The investigated capacity for this study relates to the value obtained of the complete discharge during the second capacity test. Afterward, three pulse tests were carried out at SOC = 80%, 50%, and 20% with a current rate of 1C, 2C, and 4C in charge and discharge direction. The SOC was

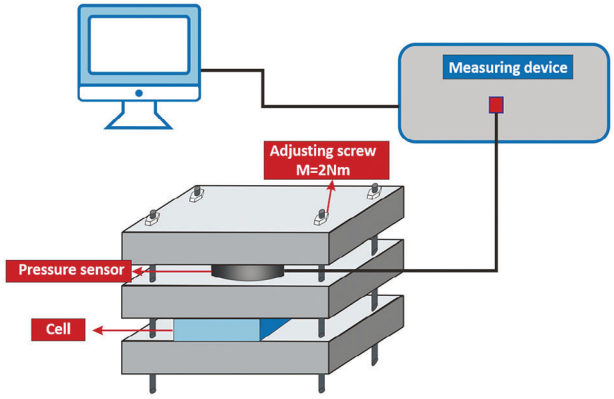

Figure 7. Illustration of the compression setup.

targeted based on the last discharge capacity measured and with a C-rate of C/3. Additionally, all initial, final and pressurized characterization tests contained a low current measurement in charge and discharge direction at a C-rate of C/10 until the respective cut-off voltages were reached. A RPT was performed after each 400 EFC for continuously pressurized cells in either pristine or aged state.

Incremental Capacity Analysis: In order to draw conclusions about the initial characteristics of the cell and later investigate the effects of long-term aging, the IC analysis method was used. Therefore, a full discharge curve measured at a low C-rate was needed to reduce the number of kinetic artifacts. As the initially conducted low-current measurements at C/10 were omitted after the first characterization test, the C/3 discharge curves would be used to assess changes in the phases of the material using ICA. Due to the high-power capability of these LTO cells, only small kinetic artifacts will remain at moderate C rates, making the C/3 discharge curve suitable for further analysis.

Post-Mortem Analysis: For the post-mortem analysis, the cells were discharged to the lower cut-off voltage of 1.5V. All post-mortem analyses were performed under an inert argon atmosphere (O2 concentration < 0.5 ppm, H2O concentration < 0.5 ppm) in a glove box. The optical investigation was performed by scanning the cells in a flatbed scanner (Canon LiDE 300). The electrode sheets from the aged cells were examined using a scanning electron microscope (Zeiss Supra 55) in combination with an energy-dispersive X-ray spectroscopy detector (Oxford Xplore 30). Therefore, two samples of each electrode with a diameter of 10 mm were punched out. The harvested electrode material was sealed in an aluminum pouch bag under vacuum in an inert argon atmosphere, and then stored for several months prior to SEM analysis. In order to analyze the balancing of the investigated cell, pristine anode and cathode material was harvested, and coin cells were built in a half-cell configuration. Therefore, the respective material extracted from the cell opening was initially decoated on one side before electrode disc probes with 16 mm diameter were punched out. The specific cathode materials (LCO and NMC) utilized in the analyzed blend cathode (NMC-LCO) were stock material obtained from earlier performed cell disassemblies of different cells. High-purity lithium metal discs with 16 mm diameter were used as counter electrodes. Whatman GF/C separators, which were punched into 17 mm discs, were used as separators. The separator was 1 mm larger in diameter to prevent the anode and the cathode of the half-cell from making direct contact at the edge area. During the assembly of the coin cells, the separator was soaked with LP57 electrolyte (90 µL, 1 M LiPF6 in 3:7 EC/EMC). In addition, a spring was embedded into the coin cell to ensure even pressure and electrolyte distribution. The coin cells were cycled at room temperature using a Neware CT-4008T-5V-10mA cycler. After an initial rest period of 24 h, three consecutive cycles with 0.09 $mAcm^{-2}$ are performed, which took ≈25 h in either the charge and discharge direction. The cut-off voltages were chosen between 3.2 and 4.5 V for all cathode half-cells (NMC versus Li/Li^+, LCO versus Li/Li^+ and blend NMC-LCO versus Li/Li^+), respectively, 1.35 and 1.75 V for the anode half-cell (LTO versus. Li/Li^+). For inductively coupled plasma optical emission spectroscopy (ICP-OES) analysis, the Varian 725-ES ICP-OES was used. For this purpose, three 20 mm stampings per aging condition were punched out of the electrode. When selecting the punch positions, attention was paid to ensure that the same age condition was present on both sides of the punched electrode.

Electrochemical Impedance Spectroscopy (EIS): EIS measurements were performed on the cells using an EISmeter within a Binder MK53 at 25°C. The frequency range of the measurements is between 6 kHz and 10 mHz and performed over the entire SOC range (0–100% SOC) in Δ SOC = 5% steps. A rest period of at least 40 min is applied after each EIS measurement to ensure the relaxation process of the cell. Afterward, an ECM was fitted to the results obtained from the EIS measurements, see **Figure 8**. R_0 describes the ohmic resistance and was quantified as the intersection of the EIS spectrum with the real axis at high frequencies. Constant phase elements (*CPEs*) were used here to model the depressed semicircles in the Nyquist plots instead of a capacitor. R_1 and CPE_1 represent the charge transfer resistance, respectively, the double layer capacity. R_2 and CPE_2 were used to represent the slow process of lithium-ion diffusion into the active material structure, as the behavior of the semi-infinite diffusion Warburg model was not ideal. The mathematical expression of the impedance for the whole ECM is

$$Z_{ECM} = R_0 + \frac{R_1}{1 + R_1 Q_1 (j\omega)^{\alpha_1}} + \frac{R_2}{1 + R_1 Q_2 (j\omega)^{\alpha_2}} \quad (2)$$

Q is the amplitude and also called the fractional coefficient, $j = (-1)^{\frac{1}{2}}$, ω is the angular frequency, α is the fractional exponent, also called the depression factor, ranging from 0 to 1. The *CPE* equals a resistance when $\alpha = 0$ and represents a capacitance when $\alpha = 1$.

Linear Regression Fitting: A linear regression model was employed to analyze the relationship between several variables. The model assumes a linear association, aiming to minimize the sum of squared differences between the observed and the predicted values generated by the linear function. Mathematically, it can be expressed as:

$$Y = \beta_0 + \beta_1 \cdot X_1 \quad (3)$$

where Y represents the dependent variable, X_1 denotes the independent variables, β_0, β_1 are the model coefficients to be estimated.

The coefficients β_0, β_1 are determined through a process that minimizes the residual sum of squares. The model accuracy and goodness of fit were assessed using the R-squared (R^2) metric.

Electrochemical Testing: Cycling under continuous pressure of pristine cells was performed at a C-rate of 3C in charge and discharge direction with a DOD of 80% between 10% and 90% SOC at an ambient temperature of 45°C. Two specimens for each condition were used. The investigated cells during transient pressure were previously aged unpressurized at different operation conditions by varying storage temperature, SOC, DOD as well as C-rate (see Ref. [54]). After a certain level of degradation was reached, cells were disconnected from the calendar and cyclic aging setup. The cells were then subjected to a RPT to retrieve information about the current cell status. Afterward, the cells were pressurized with 0.3 MPa and the aforementioned RPT is repeated on the pressurized cells. Continuously pressurized cycling for aged cells was conducted similarly to that of pristine cells, under varying stress conditions, as described in Section 2.4. Subsequently, intermittent pressure is applied by pressurizing the cells, performing a RPT, withdrawing the pressure, and performing another RPT multiple times.

Throughout this study, all shown capacity values were normalized to the extracted capacity initially measured at C/3. Similarly, the values for the inner resistances were normalized to the initial 10 s 4C discharge pulse resistance at 50% SOC. The relative capacity recovery values were calculated by subtracting the capacity extracted under transient pressure (C_p) from the amount of available capacity after unpressurized aging but before pressurization (C_a) and dividing the result by the initially available capacity (C_{init}) of the respective pristine cell, see Equation (5). The SOH is accord-

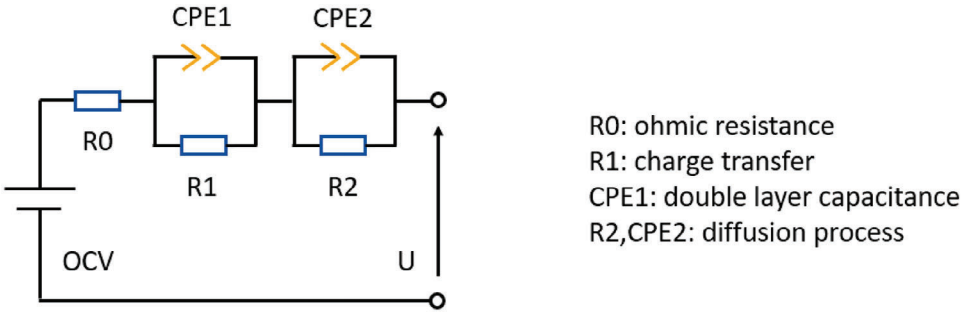

Figure 8. Overview of the ECM used to fit the obtained impedance data.

ingly defined for all capacity values presented in this paper, according to Equation (4).

$$SOH_{\{p,a\}} = \frac{C_{\{p,a\}}}{C_{init}} \cdot 100\% \tag{4}$$

$$Capacity\ recovery = \frac{C_p - C_a}{C_{init}} \cdot 100\% = SOH_p - SOH_a \tag{5}$$

Supporting Information

Supporting Information is available from the Wiley Online Library or from the author.

Acknowledgements

This work was funded by the German Federal Ministry for Transport and Digital Infrastructure (BMVI) within the project XEMU and with the funding numbers 03B10502B and 03B10502B2 and the German Federal Ministry of Education and Research (BMBF), within the project BALd and the funding number 03XP0320A.

Open access funding enabled and organized by Projekt DEAL.

Conflict of Interest

The authors declare no conflict of interest.

Data Availability Statement

The data that support the findings of this study are available on request from the corresponding author. The data are not publicly available due to privacy or ethical restrictions.

Keywords

battery, aging, capacity recovery, lithium titanate oxide, post-mortem, pressure, prismatic cells

Received: October 11, 2024
Published online:

[1] L. Al-Ghussain, *Environ. Prog. Sustainable Energy* **2019**, *38*, 13.
[2] R. R. Kumar, K. Alok, *J. Cleaner Prod.* **2020**, *253*, 119911.
[3] J. Gao, Y. Li, L. Shi, J. Li, G. Zhang, *ACS Appl. Mater. Interfaces* **2018**, *10*, 20635.
[4] Y. Ding, Z. P. Cano, A. Yu, J. Lu, Z. Chen, *Electrochem. Energy Rev.* **2019**, *2*, 1.
[5] A. Farmann, W. Waag, D. U. Sauer, *Energy* **2016**, *112*, 294.
[6] M. Dubarry, B. Y. Liaw, *J. Power Sources* **2009**, *194*, 541.
[7] F. Rücker, I. Schoeneberger, T. Wilmschen, A. Chahbaz, P. Dechent, F. Hildenbrand, E. Barbers, M. Kuipers, J. Figgener, D. U. Sauer, *Energies* **2022**, *15*, 4186.
[8] S. Käbitz, J. Tübke, D. U. Sauer, *Untersuchung der alterung von lithium-ionen-batterien mittels elektroanalytik und elektrochemischer impedanzspektroskopie*, Technical report, Institut für Stromrichtertechnik und Elektrische Antriebe, Aachen, Germany **2016**.
[9] L. Spitthoff, P. R. Shearing, O. S. Burheim, *Energies* **2021**, *14*, 1248.
[10] N. I. Nikolov, A. Chahbaz, F. Hildenbrand, M. Kateri, D. U. Sauer, *J. Power Sources* **2024**, *623*, 235334.
[11] L. Cloos, O. Queisser, A. Chahbaz, S. Paarmann, D. U. Sauer, T. Wetzel, *Batter. Supercaps* **2024**, *7*, e202300445.
[12] H. Chen, A. Chahbaz, S. Yang, W. Zhang, D. U. Sauer, W. Li, *eTransportation* **2024**, *21*, 100340.
[13] A. Barai, Y. Guo, A. McGordon, P. Jennings, *Int. Conf. on Connected Vehicles and Expo (ICCVE)*, IEEE, New York **2013**, pp. 295–299.
[14] T. C. Bach, S. F. Schuster, E. Fleder, J. Müller, M. J. Brand, H. Lorrmann, A. Jossen, G. Sextl, *J. Energy Storage* **2016**, *5*, 212.
[15] J. Cannarella, C. B. Arnold, *J. Power Sources* **2014**, *245*, 745.
[16] A. S. Mussa, M. Klett, G. Lindbergh, R. W. Lindström, *J. Power Sources* **2018**, *385*, 18.
[17] V. Müller, R.-G. Scurtu, M. Memm, M. A. Danzer, M. Wohlfahrt-Mehrens, *J. Power Sources* **2019**, *440*, 227148.
[18] G. Berckmans, L. De Sutter, M. Marinaro, J. Smekens, J. Jaguemont, M. Wohlfahrt-Mehrens, J. Van Mierlo, N. Omar, *Electrochim. Acta* **2019**, *306*, 387.
[19] A. Epp, D. U. Sauer, *Energy Technol.* **2022**, *10*, 2100874.
[20] P. Daubinger, M. Schelter, R. Petersohn, F. Nagler, S. Hartmann, M. Herrmann, G. A. Giffin, *Adv. Energy Mater.* **2022**, *12*, 2102448.
[21] L. De Sutter, G. Berckmans, M. Marinaro, M. Wohlfahrt-Mehrens, M. Berecibar, J. Van Mierlo, *J. Power Sources* **2020**, *451*, 227774.
[22] Y. Zhou, *Curr. Opin. Electrochem.* **2022**, *31*, 100916.
[23] M. Kitta, T. Akita, S. Tanaka, M. Kohyama, *J. Power Sources* **2013**, *237*, 26.
[24] N. Takami, H. Inagaki, Y. Tatebayashi, H. Saruwatari, K. Honda, S. Egusa, *J. Power Sources* **2013**, *244*, 469.
[25] Y.-B. He, B. Li, M. Liu, C. Zhang, W. Lv, C. Yang, J. Li, H. Du, B. Zhang, Q.-H. Yang, J.-K. Kim, F. Kang, *Sci. Rep.* **2012**, *2*, 1.
[26] M. Wagemaker, E. R. van Eck, A. P. Kentgens, F. M. Mulder, *J. Phys. Chem. B* **2009**, *113*, 224.
[27] D. Young, A. Ransil, R. Amin, Z. Li, Y.-M. Chiang, *Adv. Energy Mater.* **2013**, *3*, 1125.

[28] A. Devie, M. Dubarry, B. Y. Liaw, *J. Electrochem. Soc.* **2015**, *162*, A1033.
[29] A. Devie, M. Dubarry, H.-P. Wu, T.-H. Wu, B. Y. Liaw, *J. Electrochem. Soc.* **2016**, *163*, A2611.
[30] Z. Mao, M. Farkhondeh, M. Pritzker, M. Fowler, Z. Chen, *J. Electrochem. Soc.* **2017**, *164*, A3469.
[31] B. P. Matadi, S. Geniès, A. Delaille, T. Waldmann, M. Kasper, M. Wohlfahrt-Mehrens, F. Aguesse, E. Bekaert, I. Jiménez-Gordon, L. Daniel, X. Fleury, M. Bardet, J,-F. Martin, Y. Bultel, *J. Electrochem. Soc.* **2017**, *164*, A1089.
[32] T. Bank, L. Alsheimer, N. Löffler, D. U. Sauer, *J. Energy Storage* **2022**, *51*, 104201.
[33] J. P. Schmidt, H. Y. Tran, J. Richter, E. Ivers-Tiffée, M. Wohlfahrt-Mehrens, *J. Power Sources* **2013**, *239*, 696.
[34] G. Baure, A. Devie, M. Dubarry, *J. Electrochem. Soc.* **2019**, *166*, A1991.
[35] Y. Ha, S. E. Trask, Y. Zhang, A. N. Jansen, A. Burrell, *J. Electrochem. Soc.* **2023**, *170*, 050520.
[36] M. Dubarry, D. Anseán, *Front. Energy Res.* **2022**, *10*, 1023555.
[37] T. Nordh, R. Younesi, D. Brandell, K. Edström, *J. Power Sources* **2015**, *294*, 173.
[38] W. Lv, J. Gu, Y. Niu, K. Wen, W. He, *J. Electrochem. Soc.* **2017**, *164*, A2213.
[39] Y.-B. He, M. Liu, Z.-D. Huang, B. Zhang, Y. Yu, B. Li, F. Kang, J.-K. Kim, *J. Power Sources* **2013**, *239*, 269.
[40] M.-S. Song, R.-H. Kim, S.-W. Baek, K.-S. Lee, K. Park, A. Benayad, *J. Mater. Chem. A* **2014**, *2*, 631.
[41] R. Dedryvère, D. Foix, S. Franger, S. Patoux, L. Daniel, D. Gonbeau, *J. Mater. Chem. C* **2010**, *114*, 10999.
[42] K. Wang, F. Gao, Y. Zhu, H. Liu, C. Qi, K. Yang, Q. Jiao, *Energy* **2018**, *149*, 364.
[43] Y.-B. He, F. Ning, B. Li, Q.-S. Song, W. Lv, H. Du, D. Zhai, F. Su, Q.-H. Yang, F. Kang, *J. Power Sources* **2012**, *202*, 253.
[44] F. Lin, I. M. Markus, D. Nordlund, T.-C. Weng, M. D. Asta, H. L. Xin, M. M. Doeff, *Nat. Commun.* **2014**, *5*, 1.
[45] C. Mao, R. E. Ruther, L. Geng, Z. Li, D. N. Leonard, H. M. Meyer III, R. L. Sacci, D. L. Wood III, *ACS Appl. Mater. Interfaces* **2019**, *11*, 43235.
[46] C. Rahe, S. T. Kelly, M. N. Rad, D. U. Sauer, J. Mayer, E. Figgemeier, *J. Power Sources* **2019**, *433*, 126631.
[47] B. Stiaszny, J. C. Ziegler, E. E. Krauß, J. P. Schmidt, E. Ivers-Tiffée, *J. Power Sources* **2014**, *251*, 439.
[48] T. Li, X.-Z. Yuan, L. Zhang, D. Song, K. Shi, C. Bock, *Electrochem. Energy Rev.* **2020**, *3*, 43.
[49] H. Arai, M. Tsuda, K. Saito, M. Hayashi, Y. Sakurai, *J. Electrochem. Soc.* **2002**, *149*, 4A401.
[50] D. H. Doughty, E. P. Roth, *Electrochem. Soc. Interface* **2012**, *21*, 37.
[51] X. Zhang, B. Peng, L. Zhao, G. Wan, F. Wang, S. Zeng, H. Zhang, J. Ding, G. Zhang, *ACS Appl. Mater. Interfaces* **2022**, *14*, 16204.
[52] H. Gabrisch, Y. Ozawa, R. Yazami, *Electrochim. Acta* **2006**, *52*, 1499.
[53] V. Muller, R. Scurtu, K. Richter, T. Waldmann, M. Memm, M. Danzer, M. Wohlfahrt-Mehrens, *J. Electrochem. Soc.* **2019**, *166*, A3796.
[54] A. Chahbaz, F. Meishner, W. Li, C. Ünlübayir, D. U. Sauer, *Energy Storage Mater.* **2021**, *42*, 794.
[55] X. Han, M. Ouyang, L. Lu, J. Li, Y. Zheng, Z. Li, *J. Power Sources* **2014**, *251*, 38.
[56] Y. Lyu, X. Wu, K. Wang, Z. Feng, T. Cheng, Y. Liu, M. Wang, R. Chen, L. Xu, J. Zhou, Y. Lu, B. Guo, *Adv. Energy Mater.* **2021**, *11*, 2000982.
[57] R. Amin, Y.-M. Chiang, *J. Electrochem. Soc.* **2016**, *163*, A1512.
[58] P. Svens, R. Eriksson, J. Hansson, M. Behm, T. Gustafsson, G. Lindbergh, *J. Power Sources* **2014**, *270*, 131.
[59] V. Charbonneau, A. Lasia, G. Brisard, *J. Electroanal. Chem.* **2020**, *875*, 113944.
[60] N. Takami, K. Hoshina, H. Inagaki, *J. Electrochem. Soc.* **2011**, *158*, A725.
[61] J. Ma, C. Wang, S. Wroblewski, *J. Power Sources* **2007**, *164*, 849.
[62] J. Illig, J. P. Schmidt, M. Weiss, A. Weber, E. Ivers-Tiffée, *J. Power Sources* **2013**, *239*, 670.
[63] X. Bai, T. Li, Y.-J. Bai, *Dalton Trans.* **2020**, *49*, 10003.